From hydroplastic to brittle deformation: Controls on fluid flow in fold and thrust belts. Insights from the Lower Pedraforca thrust sheet (SE Pyrenees)

David Cruset, Irene Cantarero, Antonio Benedicto, Cedric M. John, Jaume Vergés, Richard Albert, Axel Gerdes, Anna Trave

From hydroplastic to brittle deformation: controls on fluid flow in fold and thrust belts. Insights from the Lower Pedraforca thrust sheet (SE Pyrenees)

David Cruset[1,4], Irene Cantarero[1], Antonio Benedicto[2], Cédric M. John[3], Jaume Vergés[4], Richard Albert[5,6], Axel Gerdes[5,6], Anna Travé[1]

[1] Departament de Mineralogia, Petrologia i Geologia Aplicada, Facultat de Ciències de la Terra, Universitat de Barcelona, (UB), Martí i Franquès s/n, 08028, Barcelona, Spain.
i_cantarero@ub.edu, atrave@ub.edu

[2] UMR Geops, Université Paris Sud, 91405 Orsay, France.
antonio.benedicto@u-psud.fr

[3] Department of Earth Science and Engineering, Imperial College London, SW7 2BP, UK.
cedric.john@imperial.ac.uk

[4] Group of Dynamics of the Lithosphere (GDL). Institut de Ciències de la Terra Jaume Almera, ICTJA-CSIC, Lluís Solé i Sabaris s/n, 08028 Barcelona, Spain.
dcruset@ictja.csic.es, jverges@ictja.csic.es

[5] Department of Geosciences, Goethe-University Frankfurt, 60438 Frankfurt am Main, Germany.
gerdes@em.uni-frankfurt.de, albertroper@em.uni-frankfurt.de

[6] Frankfurt Isotope and Element Research Center (FIERCE), Goethe-University Frankfurt, Frankfurt am Main, Germany.

Abstract

We present a multidisciplinary study to decipher the controls of deformation on fluid flow regime in fold and thrust belts using the Lower Pedraforca thrust sheet in the SE Pyrenees as an example. We integrate field-based and petrographic observations and geochemical and geochronological data to differentiate seven types of fractures, eight types of calcite cement (Cc1 to Cc8) and two sets of stylolites during the deformation stretching the studied thrust sheet.

During syn-sedimentary hydroplastic normal faulting affecting poorly consolidated Upper Cretaceous and Eocene syn-orogenic sediments, calcite cement did not precipitate. During burial, bed-parallel stylolites formed and Cc1 and Cc2 precipitated from formation waters in a closed palaeohydrological system. During the layer-parallel shortening, Cc3 precipitated from formation waters (~+5.4 ‰ VSMOW) with $^{87}Sr/^{86}Sr$ ratios of 0.707922 and at ~70 ºC. Cc4 precipitated from formation waters recording different burial conditions, as the up to 4 ‰ dispersion in $\delta^{18}O$ of this cement suggests. Contrarily, during folding and thrusting, Cc5 to Cc7 precipitated in an open palaeohydrological system. Cc6

precipitated from formation waters (~+5 ‰ VSMOW), with $^{87}Sr/^{86}Sr$ ratios of 0.707817 and at ~75 ºC. These fluids carried hydrocarbons and probably interacted with Upper Triassic evaporites. An $^{87}Sr/^{86}Sr$ ratio of 0.708230 for Cc5 indicates that formation waters also interacted with clays within continental deposits. During this period, stylolites formed in relation to faulting, and previous hydroplastic normal faults reactivated as reverse and strike-slip faults allowing fluid flow. Cc7 precipitated after Cc6, also from fluids in isotopic disequilibrium with their adjacent host rock. The fluid system continued open during the Oligocene, when Cc8 precipitated in normal faults affecting syn-orogenic conglomerates deposited during the reactivation of the Lower Pedraforca thrust sheet.

The influence of deformation on fluid flow observed in the Lower Pedraforca thrust sheet is similar to that observed in other fractured areas worldwide.

Keywords: Hydroplastic and brittle deformation, fluid flow, U-Pb calcite dating, clumped isotopes, fold and thrust belts.

1. Introduction

The study of fracture-filling cement in fold and thrust belts reveals changes in the fluid regime and the evolution of fluid-rock interaction through time (Vandeginste et al., 2007, 2012; Breesch et al., 2009; Beaudoin et al., 2014; Crognier et al., 2018; Cantarero et al., 2018; Cruset et al., 2018). In the shallow crust, brittle deformation is responsible for the formation of fractures (Marrett and Allmendinger, 1990), which act as preferential conduits or seals for the migration of fluids (Missenard et al., 2014; Ogata et al., 2014; Maher et al., 2017). However, the conduit or barrier behaviour is not steady-state and it can evolve through time, especially due to: 1) variations in the stress field, forcing changes in the tectonic regime (Sibson, 1995; Wiprut and Zoback, 2000; Soumaya et al., 2015); 2) the increase of fluid pressure, which can produce seismically-induced slip and/or hydraulic fracturing (Aydin, 2000; Wiprut and Zoback, 2000; Rutqvist et al., 2013); 3) fracture sealing by cement due to fluid regime changes (temperature, pressure,

composition; Benedicto et al., 2008; Beaudoin et al., 2014); and 4) a combination of these factors.

The reactivation of faults can increase the heterogeneity of fractured reservoirs and the uncertainty during reservoir analysis (Roure et al., 2005; Casini et al., 2011; Khosravi et al., 2012; Tavani et al., 2015). Moreover, these heterogeneities are also controlled by additional factors such as fault core composition and strain distribution during folding, which also affects fault permeability (Egholm et al., 2000; Dimmen et al., 2017; Watkins et al., 2018). The study of these factors in outcrop analogues is key to mitigate the uncertainties related to the evaluation of fractured reservoirs with bad accessibility and those that are under exploration or production stages.

The southern Pyrenees is an exceptionally well-preserved fold and thrust belt in which the complete sequence of thrust sheets and the age of their related syn-tectonic deposits are well known (e.g., Vergés et al., 2002). In this compressional belt, the relationships between fluid migration and deformation have been studied either in its Palaeozoic basement (McCaig et al., 1995, 2000; Trincal et al., 2017), cover thrust sheets constituted of Mesozoic and Palaeogene rocks (Travé et al., 1997, 1998; Beaudoin et al., 2015; Crognier et al., 2018; Cruset et al., 2018; Lacroix et al., 2014, 2018; Nardini et al., 2019) and in its foreland basin, constituted of Palaeogene rocks (Travé et al., 2000; Cruset et al., 2016). Other studies in the southern Pyrenees report the presence of fractures formed in hydroplastic (Soliva and Benedicto, 2004, 2005; Soliva et al., 2006, 2008) and brittle (Shackleton et al., 2005, 2011; Tavani et al., 2011; Gutmanis et al., 2017) regimes. However, the relationships between fluids and hydroplastic fractures, as well as their evolution through time, have not been studied yet in the southern Pyrenees.

In this contribution, we report a whole history of fluid flow evolution from syn-sedimentary hydroplastic deformation to later brittle fracturing in a section of a fold and thrust belt, which includes reactivation of pre-compressive structures. To deal with the aim of this study, we use the Lower Pedraforca thin-skinned thrust sheet in the SE Pyrenees as an

example of a fractured reservoir that increases its heterogeneity during progressive folding. The exceptional outcrop exposures of this thrust sheet allowed to work on three meso-scale (metre-scale) fracture systems that are correlative through time: 1) hydroplastic normal faults (as defined by Petit and Beauchamp (1986) and Petit and Laville (1987); 2) background fracture systems, which consist of stratabound bed-perpendicular veins and bed-parallel slip surfaces; and 3) non-stratabound fracture systems formed of reverse, strike-slip and normal faults. The study of the evolution of these fracture systems is combined with petrographic observations and geochemical data (carbon, oxygen and strontium isotopes, clumped isotopes thermometry, elemental composition and U-Pb geochronology) of fracture-filling calcites, extending the fluid flow history reported previously by Cruset et al. (2018) for the Lower Pedraforca thrust sheet. The results obtained will be compared with other fractured areas worldwide.

2. Geological setting

The Pyrenees (Fig. 1A) formed due to the continental collision that resulted from the partial subduction of the Iberian plate beneath the Eurasian plate from Late Cretaceous to Miocene (Choukroune et al., 1989; Roure et al., 1989; Muñoz, 1992; Vergés et al., 2002). As a result, the previous Mesozoic rift basins were inverted, and an antiformal stack of thrust sheets constituted of basement units (the Axial Zone) developed along the internal zone of the Pyrenean doubly verging orogenic system (Fig. 1B), acting as a boundary between the north and south Pyrenean fold and thrust belts (e.g., Muñoz, 1992; Grool et al., 2018).

The south Pyrenean fold and thrust belt (Fig. 1B, C, and 2A) consists of a piggy-back sequence of south-verging thrusts (e.g., Puigdefàbregas et al., 1992), detached predominantly above Upper Triassic (Séguret, 1972) and Eocene evaporites deposited in the foreland basin (Vergés et al., 1992; Sans et al., 1996). In this work, we study the Lower Pedraforca thrust sheet (Fig. 1C and 2A), which emplaced from Lower to Middle Eocene using a detachment level located in the Upper Triassic Keuper facies

(Puigdefàbregas et al., 1986; Burbank et al., 1992a). The emplacement of this structural unit took place under marine foreland conditions, as attested by the syn-orogenic fan delta conglomerates of Queralt deposited at the thrust front (Vergés, 1993).

The complete stratigraphy of the Lower Pedraforca thrust sheet constitutes a sedimentary wedge of up to 2400 m in the northern imbricate and less than 500 m in the frontalmost thrust nappes (Vergés 1993; Fig. 1C). This stratigraphy ranges in age between the Upper Triassic and the Oligocene and consists of pre- to syn-orogenic sedimentary rocks (Fig. 2B). Pre-compressive stratigraphy consists of evaporites and red clays from the Keuper facies, Jurassic limestones and dolostones from the Bonansa Formation and Coniacian to Lower Santonian limestones from the Sant Corneli Formation (Mey et al., 1968; Simó, 1985; Calvet et al., 1993). Syn-orogenic deposits comprise Late Cretaceous, Eocene and Oligocene detrital rocks. Late Cretaceous rocks comprise upper Santonian to Campanian marine sandstones and limestones from the Vallcarga Formation, Campanian-Maastrichtian coastal deposits of the Areny Formation and Maastrichtian-Thanetian continental deposits from the Garumnian (Moeri, 1977; López-Martínez et al., 1999; Rosell et al., 2001; Oms et al., 2007). Eocene rocks comprise lower Ypresian limestones from the Cadí Formation, the upper Ypresian to Lutetian marine conglomerates of Queralt, and middle Lutetian to Bartonian conglomerates of the Coubet Formation (Solé Sugrañes and Clavell, 1973). Eocene-Oligocene continental conglomerates deposited during the reactivation of the northern margin of the Lower Pedraforca thrust sheet (Vergés, 1993).

3. Methodology

Five localities (Q, G1, PEG, G2 and EST) located in the southern (Q, G1) and the northern (G2, EST) margins and in the internal nappes forming the Lower Pedraforca thrust sheet (PEG) were chosen to study the structural controls on fluid flow during the development of this structure (Fig. 2).

144 Bedding and fractures were measured in the field, and their crosscutting relationships
145 were recorded. The fracture analysis was carried out using the program Win-Tensor
146 (v5.8.8.) (Delvaux and Sperner, 2003). Restoration of fracture data and associated stress
147 orientations with respect to their adjacent bedding has been done using the same
148 software. Each fracture system is plotted in Lower hemisphere Schmidt stereoplots, and
149 their associated stresses are also calculated with the same software. Additionally,
150 sampling of 58 fracture-filling calcite cement and related host rocks was undertaken for
151 petrographic observations and geochemical analyses.

152 Petrographic observations of 57 polished thin sections made from six different host rocks
153 and eight types of fracture-filling calcite cement were made using optical and
154 cathodoluminescence microscopy. A CL Technosyn cathodoluminescence device Model
155 8200 MkII at 15-18 kV operating conditions and 350 µA gun current was used to
156 distinguish the different types of cement.

157 The U-Pb dating method was applied to determine the absolute timing of fluid migration
158 and fracturing. This method is similar to that previously described by Ring and Gerdes
159 (2016) and Burisch et al. (2017). U-Pb dates were acquired using laser ablation-
160 inductively coupled plasma mass spectrometry (LA-ICPMS) at FIERCE (Frankfurt
161 Isotope and Element Research Center, Goethe Universität), applying a modified method
162 of Gerdes and Zeh (2006, 2009). A ThermoScientific Element XR sector field ICPMS
163 was coupled to a RESOlution 193nm ArF excimer laser (COMpexPro 102) equipped with
164 a two-volume ablation cell (Laurin Technic S155). Samples were ablated in a helium
165 atmosphere (300 mL/min) and mixed in the ablation funnel with 1100 mL/min argon and
166 5 mL/min nitrogen. Signal strength at the ICP-MS was tuned for maximum sensitivity,
167 whereas keeping the oxide formation (monitored as $^{248}ThO/^{232}Th$) below 0.2% and no
168 fractionation of the Th/U ratio. Static ablation used a spot size of 213 µm and a fluency
169 of about 2 J/cm at 12 Hz. For NIST SRM 614 this yielded a depth penetration of ~0.6
170 µm/s and an average sensitivity of 380,000 cps/µg for ^{238}U. The detection limit for ^{206}Pb

and ^{238}U was ~0.2 and 0.03 ppb, respectively. Data were acquired in fully automated mode overnight in three sequences of 598 analyses each. Each analysis consisted of 18 s of background acquisition followed by 18 s of sample ablation and 25 s of washout. During 36 s of data acquisition, the signal of ^{206}Pb, ^{207}Pb, ^{208}Pb, ^{232}Th, and ^{238}U was detected by peak jumping in pulse-counting and analog mode with a total integration time of ~0.1s, resulting in 370 mass scans. Prior to analysis, each spot was pre-ablated with 8 laser pulses to remove surface contamination. Soda-lime glass NIST SRM 614 was used as a primary reference together with three carbonate reference materials, which were bracketed in between the analysis of samples (see Table S4 for validation results). Raw data were corrected offline using an in-house VBA spreadsheet program (Gerdes and Zeh, 2006, 2009). Following background correction, outliers (±2σ) were rejected based on the time-resolved $^{207}Pb/^{206}Pb$ and $^{206}Pb/^{238}U$ ratios. The mean $^{207}Pb/^{206}Pb$ ratio of each analysis was corrected for mass bias 0.3% and the $^{206}Pb/^{238}U$ ratio for inter-element fractionation (~5%), including drift over the sequence time, using SRM 614. Due to the carbonate matrix, additional offset factors were applied (sequence 1: 1.06, sequence 2: 0.96 and sequence 3: 1.10), which were determined using WC-1 carbonate reference material (Roberts et al., 2017). The $^{206}Pb/^{238}U$ fractionation during 20s depth profiling was estimated to be 3%, based on the common Pb corrected WC-1 analyses, and was applied as an external correction to all carbonate analyses. Uncertainties were calculated by quadratic addition of the standard deviation of the mean of the considered isotopic ratios, the counting statistic uncertainties of each isotope, the uncertainty of the primary reference material after drift correction, and the decay constants uncertainties. The mean square of weighted deviates (MSWD) for the WC-1 lower intercept age of each analytical session was about 0.52 to 1.50. Thus, no carbonate matrix-related excess of variance was included in the uncertainty propagation. Reference material ASH15 (3.085 ± 0.044 and 3.005 ± 0.026 Ma; Vaks et al., 2003) was measured. In addition, a stromatolitic limestone from the Cambrian-Precambrian boundary in South-Namibia (here called NAMA) was analysed, and used as a secondary in-house RM for

quality control (obtained ages agree with the U/Pb zircon age of 540.1 ± 0.1 Ma from the directly overlying ash layer, Spitskopf formation; Linnemann et al. 2018). Altogether the data imply an accuracy and repeatability of the method of ~2%. The analytical results are presented in Tables S3 and S4. Data were plotted in Tera-Wasserburg diagrams and ages were calculated as lower intercepts using Isoplot 3.71 (Ludwig, 2009). All uncertainties are reported at the 2σ level.

For carbon and oxygen stable isotope analysis of calcite cement and carbonate host rocks, a 400 µm-thick dental drill was employed to extract 60 ± 10 µg of carbonate powder from trims. The calcite powder was reacted with 100% phosphoric acid for 2 minutes at 70 °C. The resultant CO_2 was analysed using an automated Kiel Carbonate Device attached to a Thermal Ionization Mass Spectrometer Thermo Electron (Finnigan) MAT-252 following the method of McCrea (1950). The International Standard NBS-18 and the internal standard RC-1, traceable to the International Standard NBS-19, were used for calibration. The results were corrected using the standard technique from Craig and Gordon (1965) and Claypool et al. (1980), expressed in ‰ with respect to the VPDB (Vienna Pee Dee Belemnite) standard. Standard deviation is ±0.02 ‰ for $\delta^{13}C$ and ± 0.05 ‰ for $\delta^{18}O$.

Clumped isotope thermometry was applied to two fracture-filling calcites to calculate temperatures of cement precipitation as well as the $\delta^{18}O$ values of the fluids from which calcite cement precipitated. The two analysed samples (Q2 and Q24) are representative of calcite cement Cc3 and Cc6. To analyse them, 2–3 mg aliquots from each cement were measured with the Imperial Batch Extraction system (IBEX), an automated line developed at Imperial College of London. Each sample was dropped in 105% phosphoric acid at 90 ºC and reacted for 30 min. The reactant CO_2 was separated using a poropak-Q column and transferred into the elbows of a Thermo Scientific MAT 253 mass spectrometer (Thermo Fisher GmbH, Bremen, Germany). The characterization of a replicate consisted of 8 acquisitions in dual inlet mode with 7 cycles per acquisition. The

post-acquisition processing was completed with a software for clumped isotope analysis named Easotope (John and Bowen, 2016). Δ_{47} values were corrected for isotope fractionation during phosphoric acid digestion employing a phosphoric acid correction of 0.069 ‰ at 90 ºC for calcite (Guo et al., 2009). The data were also corrected for non-linearity applying the heated gas method (Huntington et al., 2009) and projected into the absolute reference frame of Dennis et al. (2011). Carbonate $\delta^{18}O$ values were calculated with the acid fractionation factors of Kim et al. (1997). Samples were measured three times and the average result was converted to temperatures using the calibration method of Davies and John, (2019). Calculated $\delta^{18}O$ values of the fluid are expressed in ‰ with respect to the VSMOW standard (Vienna Standard Mean Ocean Water).

One sample of host limestones and three types of fracture-filling calcites were analysed for $^{87}Sr/^{86}Sr$ isotopes. 100% carbonate samples are dissolved in 5 ml of 10% acetic acid and introduced in an ultrasonic bath for 15 minutes. After this time, samples are dried after being centrifuged during 10 min at 4000 rpm. The remaining sample is digested in 1 ml of 3 M HNO_3 and dried. Finally, the resultant product is digested again in 3 ml of 3 M HNO_3 and introduced in chromatographic columns. The chromatographic separation of Sr was done using an extraction resin type SrResinTM (Trisken International) (crown-ether (4.4' (5')-di-t-butylcyclohexano-18-crown-6). The Sr is recovered with HNO_3 0.05 M as eluent. The fraction where Sr is concentrated is dried, charged on a Re single filament with 1 µl of H_3PO_4 1 M and 2 µl of Ta_2O_5 and analysed on a TIMS-Phoenix mass spectrometer. The method of acquisition of data consists of dynamic multicollection during 10 blocks of 16 cycles each one, with a beam intensity for the ^{88}Sr mass of 3 V. Analyses were corrected for possible interferences of ^{87}Rb. The $^{87}Sr/^{86}Sr$ ratios are normalized with respect to the measured mean value of the ratio $^{86}Sr/^{88}Sr=0.1194$ in order to correct possible mass fractionation during filament charge and instrumental analyses. During sample analysis, the isotopic standard NBS-987 was measured seven times obtaining a mean value of 0.710247 and a standard deviation 2σ of 0.000008.

253 These values have been used for the correction of the analysed values in the samples.
254 The precision of the analytical standard error or internal precision is 0.000009. The
255 analytical errors referred to 2σ confidence levels in the $^{87}Sr/^{86}Sr$ ratio are 0.000003.

256 Carbon-coated polished thin sections were used to analyse major, minor, and trace
257 element concentrations on a CAMECA SX-50 electron microprobe. The microprobe was
258 operated using 20 kV of excitation potential, 15 nA of current intensity and a beam
259 diameter of 10 µm. Analytical standards included natural silicates, carbonates and oxides
260 as follows: calcite (Ca), dolomite (Mg), Fe_2O_3 (Fe), rhodonite (Mn) and Celestite (Sr).
261 The detection limits were 135 ppm for Mn, 127 ppm for Fe, 101 ppm for Ca, 146 ppm for
262 Na, 180 ppm for Mg, and 390 ppm for Sr. Precision on major element analyses averaged
263 0.64% standard error at 2σ confidence levels.

264 ## 4. Results

265 ### 4.1. Locality description

266 The five studied localities (Q, G1, PEG, G2 and EST, from south to north) belong to the
267 thrust system in the Lower Pedraforca thrust sheet (Fig. 1B and 2A). Fracture data
268 interpretation and sampling were carried out in representative localities of each exposed
269 thrust nappe.

270 The locality Q corresponds to the frontal part of the Lower Pedraforca thrust sheet, one
271 km to the north of Berga city (Fig. 2A). The general structure of this locality consists of
272 three imbricated thrust sheets constituted by the Upper Cretaceous Areny Formation and
273 the Palaeocene Garumnian red beds (Fig. 1C). To the south, the front of the thrust
274 system is unconformably overlain by the upper Ypresian to lower Lutetian conglomerates
275 of Queralt, which define a growth strata. The syn-tectonic conglomerates of Queralt are
276 unconformably overlain by the conglomerates of the Coubet Formation.

277 Localities G1 and PEG are located 3 km to the N and 10 km to the NW from Berga city,
278 along the frontal region of the Lower Pedraforca thrust sheet (Fig. 1C and 2A). In locality

279 G1, the hangingwall of the thrust is constituted of the Upper Triassic Keuper facies, which
280 gradually change upwards to the Lower Jurassic Bonansa Formation. These are
281 unconformably overlain by the Upper Cretaceous Vallcarga Formation. The footwall of
282 the thrust in locality G1 is formed by the Upper Cretaceous Vallcarga Formation. In the
283 locality PEG, a thrust fault cuts across Palaeocene Garumnian limestones in both
284 hangingwall and footwall (Fig. 1C and 2A).

285 The locality G2 is located in the northernmost part of the Lower Pedraforca thrust sheet,
286 1 km to the S of Bagà village (Fig. 1 and 2A). In this area the entire Lower Pedraforca
287 thrust sheet is folded, during the younger emplacement of the Cadí thrust sheet, and
288 dips south forming the northern flank of the Ripoll syncline (Fig. 1C). The locality G2 is
289 located along the basal thrust of the Lower Pedraforca limiting with the underlying Cadí
290 thrust sheet. The hangingwall of the basal thrust is formed by Upper Triassic Keuper
291 facies overlain by Lower Jurassic limestones, whereas the footwall is constituted by
292 middle Eocene Campdevànol Formation.

293 Finally, the locality EST is located 3 km to the NE of Gósol village (Fig. 1 and 2A). It
294 consists of Oligocene conglomerates deposited along the northern sector of the Lower
295 Pedraforca thrust sheet once eroded and latter thrusted to north during the thrust
296 reactivation during progressive folding. These conglomerates are unconformably
297 overlying the middle Eocene Armàncies Formation, belonging to the Cadí thrust sheet
298 (Fig. 2B).

299 4.2. Host rocks

300 The Lower Pedraforca thrust sheet is constituted by a thick Jurassic, Upper Cretaceous,
301 Palaeocene, Eocene, and Oligocene sedimentary successions.

302 The Jurassic Bonansa Formation consists of mudstones without skeletal components
303 and with millimetre-thick sub-horizontal lamination. The Upper Cretaceous host rocks
304 include the marine Vallcarga and Areny Formations. The Vallcarga Formation is formed

of grainstones with up to 10% of detrital quartz. Microfauna includes *Orbitoides* and *Hemicyclammina,* indicating a late Santonian age (Pons and Caus, 1996). The Areny Formation is mainly composed of grainstones of peloids, miliolids and bryozoan and echinoid fragments and changes northwards to wackestones of gastropods and algae and scleractinian coral fragments. The Palaeocene Garumnian facies consist of continental detrital and carbonate rocks. Detrital rocks include red clays with orange and purple colorations, with abundant Microcodium that occasionally replaces the whole rock and suffer dissolution processes, as well as fine-grained sandstones formed of quartz (~10%) and carbonate clasts (~80-90%). These sandstones have an excellent sorting and are well-cemented. Regarding the Garumnian carbonate deposits, they are grey-brown mudstones and wackestones with charophytes. Middle Eocene syn-orogenic sediments deposited in the Lower Pedraforca thrust front are formed of well-cemented, medium-grained grey sandstones with a good sorting. Detrital components consist of Microcodium fragments from the Garumnian (~5-10%), limestone clasts (~70%), quartz (~10%), and Nummulites (~10%). Oligocene conglomerates are formed of centimetre- to metre-scale carbonate clasts supported by a matrix constituted of well-cemented and coarse-grained sandstones with a good sorting. Detrital components of the matrix are lithics derived from carbonates (>60%) and metamorphic rocks and quartz.

4.3. Fracture analysis

The Lower Pedraforca thrust sheet was affected by up to seven fracture sets (F1 to F7) summarized in chronological order in Fig. 3. Fracture classification has been done according to the type of fracture, crosscutting relationships, angular relationships with bedding and U-Pb dating of fracture-filling calcite cement (U-Pb dates will be described in detail in the geochemistry section).

After their restoration with respect to bedding, fracture set F1 consists of E-W stratabound normal faults affecting the Upper Cretaceous Areny Formation and Middle Eocene syn-orogenic sediments deposited in the thrust front (Fig. 3). These faults dip

45º to 80º either towards the north or south, have a length of up to 2 m with millimetre thickness and they show displacements up to 10 cm and soft, undulated grooves and striae sets (Fig. 4A and B). These features are indicative of hydroplastic deformation as defined by Petit and Beauchamp (1986) and Petit and Laville (1987) and are similar to those faults described in other areas of the Lower Pedraforca thrust sheet by Soliva and Benedicto (2004, 2005), Soliva et al. (2006, 2008). Calculated stress orientations indicate an N-S extension (Fig. 3). These fractures do not have calcite cement, although occasionally calcite veins with reverse striae sets have been observed, resulted from a later reactivation. Fracture set F1 has been observed in locality Q.

The second fracture set (F2) consists of bed-parallel slip surfaces formed occasionally at the contact between clays and more competent layers of the Areny Formation and Garumnian facies in locality Q (Figs. 3 and 4C). F2 fractures have a thickness of up to 0.5 cm and a length of a few centimetres.

Fracture set F3 consists of N-S, NNW-SSE, and NNE-SSW bed-perpendicular veins that often display en-échelon arrays (Fig. 3 and 4D and E). F3 is stratabound and show sub-vertical dips after restoring bedding to the horizontal. F3 shows openings of up to 2 cm and lengths of up to 30 cm. These fractures affect the Upper Cretaceous Areny Formation, the Palaeocene Garumnian facies and the Middle Eocene syn-orogenic sediments. Calculated stress orientations for F3 indicate a N-S strike-slip motion (Fig. 3). F3 has only been observed in locality Q.

Fracture set F4 is constituted of E-W, NNE-SSW, and NNW-SSE reverse fault zones and their associate veins affecting the Jurassic and Upper Cretaceous Bonansa, Areny and Vallcarga Formations (Fig. 3 and 5A). These faults dip between 15º and 75º towards the N and NW, are not stratabound, have a constant orientation regardless of bed dips, are filled with calcite and occasionally contain hydrocarbon seeps. Fault cores are formed of thick S-C zones with the development of pressure-solution cleavage (Fig. 5B) or thin discrete planes formed of up to 2 cm-thick shear veins. F4 shows lengths from a

few centimetres to tens of meters. However, in thrust faults in which thick units of Upper Triassic evaporites act as a detachment, hydraulic fracturing is observed within the most competent limestones of the footwall (Fig. 5C). These fractured areas extend tens of meters away from the fault core. The calculated stress orientation for F4 indicates an N-S (localities G1, PEG and G2) and NW-SE (locality Q) reverse motion (Fig. 3). In locality Q, some of the reserve faults formed due to the reactivation of hydroplastic normal faults F1.

The fifth fracture set (F5) consists of N-S, NW-SE, NNW-SSE, and NE-SW strike-slip faults dipping between 45º and 90º that affect Upper Triassic, Jurassic, Upper Cretaceous, and Palaeocene rocks. Fault planes are discrete, formed of shear veins with a thickness of up to 2 cm and show striae sets indicating dextral and sinistral motion (Fig. 3 and 5D). F5 faults have lengths of up to 5 metres. Calculated stress orientations for F5 indicate NW-SE, N-S, and NE-SW strike-slip motion in localities Q, G1, G2, and EST, respectively (Fig. 3). Like F4, strike-slip faults have a constant angle regardless of bed dip.

Fractures F6 consists of 1 cm-wide and up to 5 cm-long N-S sub-vertical veins observed occasionally in thrust fault zones of the locality G1 (Fig. 3). These fractures affect folded Jurassic strata at a constant angle, indicating their late-folding formation. The stress orientation for F6 indicates NNW-SSE strike-slip motion (Fig. 3).

Fracture set F7 consists of normal faults affecting the Oligocene conglomerates related to the reactivation of the Lower Pedraforca thrust sheet studied in locality EST (Fig. 5E). These faults have an NNW-SSE strike, a dip between 60º and 80º either towards the SW and NE and show fault displacements from 1 to 2 m (Fig. 3). Fault planes are discrete, formed of up to 2 cm-thick extensional veins, and show lengths of up to 20 metres. Calculated stress orientations for F7 indicate an ENE-WSW extension.

384 4.4. Petrography

385 From petrographic observations and U-Pb geochronology, eight types of calcite cement
386 filling fracture, vug and moldic porosity (Cc1 to Cc8 in chronological order) and two sets
387 of stylolites (St1 and St2) have been identified in the Lower Pedraforca thrust sheet.
388 Their main features and crosscutting relationships are summarized in Figs. 3, 6, and 7.
389 Some of the collected samples are located in Fig. 5 for reference.

390 Calcite cement Cc1 and Cc2 are not fracture-related. Cc1 consists of non-luminescent
391 microsparite precipitated in the intergranular and moldic porosity of grainstones from the
392 Areny and Vallcarga Formations in localities Q and G1, respectively (Fig. 6A and B). Cc2
393 consists of blocky calcite crystals of more than 1 mm in size. This cement is non-
394 luminescent and precipitated in vug porosity affecting the Garumnian facies in locality Q
395 and in the intergranular porosity of breccias within the Jurassic limestones in locality G1
396 (Fig. 7). Cc3 precipitated in F2 and F3 fractures and vug porosity postdating Cc1 and
397 Cc2 in locality Q (Fig. 6A, B, and 7). This cement is orange luminescent and consists of
398 blocky calcite crystals ranging from 100 to 300 μm and fibrous calcite crystals parallel to
399 fracture walls varying from 200 μm to 2 mm in length. Blocky crystals have been
400 observed filling rhomb-shaped veinlets formed by crack-seal mechanism in F2 fractures.
401 Cc4 consists of blocky and bladed crystals ranging between 250 μm and 2 mm and
402 between 300 μm and 1 mm in length, respectively. This cement is dull-orange to orange
403 luminescent and precipitated in reactivated F1 fractures and in F3 veins affecting Eocene
404 syn-orogenic sediments in locality Q (Fig. 7). Cc5 consists of sparite crystals ranging
405 from 100 to 700 μm. This cement is zoned, from non-luminescent to dull orange and
406 precipitated in vug porosities within the Areny Formation and in some F4 fractures
407 postdating the previous cement in locality Q (Fig. 6A and B). Cc6 consists of blocky
408 microsparite and from 200 μm to 2 mm fibrous crystals arranged parallel and oblique to
409 fracture walls. Blocky sparite has been also observed filling rhomb-shaped veinlets
410 formed by crack-seal mechanism (Fig. 6C and D). Cc6 is dull-brown luminescent and

411 precipitated in vug porosities within the Areny Formation and in F4 and F5 fractures
412 postdating Cc2 and Cc5 (Fig. 7). Cc6 has been observed in localities Q, G1, G2, and
413 PEG. Cc7 consists of locally zoned blocky calcite crystals ranging from 100 μm to 1mm
414 and up to 1 mm fibrous crystals arranged perpendicular to fracture walls (Fig.7). This
415 cement is dull to bright orange and precipitated in F6 fractures. Cc7 has only been
416 observed in locality G1. Calcite cement Cc8 consists of blocky crystals ranging from 500
417 μm to more than 2 mm in size and shows orange luminescence (Fig. 6E and F). Cc8 has
418 been only observed within normal faults F7 in locality EST.

419 Stylolites St1 consist of a set of bed-parallel stylolites affecting preferentially mudstones
420 from the Jurassic Bonansa Formation and the Palaeocene Garumnian (Fig. 7). St1 are
421 postdated by Cc3 precipitated in F3 veins and have been observed in Q, G1 and G2
422 localities (Fig. 3). St2 stylolites are arranged both parallel and perpendicular to the walls
423 of F4 and F5 fractures containing Cc6. St2 stylolites occasionally affect internally Cc6
424 and occur at the contacts between this cement and its adjacent carbonate host rocks
425 (Figs. 3 and 7). Close to F4 fractures, host carbonates display stylobreccia fabrics in
426 Garumnian mudstones from locality PEG. Crosscutting relationships with Cc7 have not
427 been observed. St2 stylolites have been observed in localities Q, G1, G2 and PEG.

428 ### 4.5. Geochemistry

429 #### *4.5.1. U-Pb geochronology*

430 U-Pb dating was applied successfully to calcite cement Cc3, Cc4, Cc6, Cc7, and Cc8.
431 The results are presented in Table 1 and Fig. 3. Concordia graphs and analytical data
432 are presented in Table S1 and Fig. S1 from supplementary material, respectively.

433 Calcite cement Cc3, Cc4, Cc6, and Cc7 yielded Lutetian ages. For Cc3, dates of 47.3 ±
434 1 and 45.7 ± 1.9 Ma were obtained. However, the youngest date has a mean squared
435 weighted deviate (MSWD) higher than 2, indicating either a mixing of dates, an
436 underestimated analytical error, minor open-system behaviour, or an incomplete initial
437 equilibration of the Pb isotopes (Rasbury and Cole, 2009). Consequently, this date must

be interpreted with some caution. Cc4 has U-Pb dates of 47.9 ± 1.3 and 44.8 ± 1.4 Ma. For Cc6, U-Pb dates of 47.2 ± 0.7 Ma and 45.1 ± 1.2 were obtained, whereas Cc7 yielded two younger dates of 42.9 ± 0.9 and 42.3 ± 0.8 Ma. Finally, for Cc8, an Oligocene U-Pb date of 30.2 ± 2 Ma was obtained.

4.5.2. Carbon and oxygen stable isotopes

The carbon and oxygen stable isotopic composition of carbonate host rocks and calcite cement within the Lower Pedraforca thrust sheet is presented in Fig. 8A and Table S2. The comparison between $\delta^{18}O$ of the sampled calcite cement and their adjacent host carbonates is shown in Fig. 8B.

Lower Jurassic marine limestones have $\delta^{13}C$ ranging from -6.06 to +4 ‰ VPDB and $\delta^{18}O$ between -5.2 and -3.6 ‰ VPDB (Fig. 8A). Marine carbonates from the Upper Cretaceous Vallcarga Formation have values between +2.1 and +2.5 ‰ VPDB and $\delta^{18}O$ between -4.1 and -3.1 ‰ VPDB (Fig. 8A). Marine carbonates from the Upper Cretaceous Areny Formation have $\delta^{13}C$ between +1.5 and +1.7 ‰ VPDB and $\delta^{18}O$ between -4.5 and -3.2 ‰ VPDB (Fig. 8). Palaeocene palustrine limestones have $\delta^{13}C$ between -17.5 and -3.7 ‰ VPDB and $\delta^{18}O$ between -8.2 and -4.8 ‰ VPDB (Fig. 8A). A carbonate clast from Oligocene conglomerates has a $\delta^{13}C$ of +1.1 ‰ VPDB and a $\delta^{18}O$ of -2.8 ‰ VPDB (Fig. 8A).

Calcite cement Cc1 to Cc5 show $\delta^{13}C$ and $\delta^{18}O$ values similar to their adjacent host rocks (Fig. 8B). Cc1 has $\delta^{13}C$ of +1.5 ‰ VPDB and $\delta^{18}O$ of -5.2 ‰ VPDB (Fig. 8A). Cc2 has $\delta^{13}C$ values between -10.1 and -6.6 ‰ VPDB and $\delta^{18}O$ values between -6.5 and -5 ‰ VPDB (Fig. 8A). For Cc3, the $\delta^{13}C$ ranges between -10.8 and -0.4 ‰ VPDB and the $\delta^{18}O$ ranges between -6.4 and -3.9 ‰ VPDB (Fig. 8A). Cc4 has $\delta^{13}C$ values between -5.9 and -3.7 ‰ VPDB and $\delta^{18}O$ between -6.9 and -2.6 ‰ VPDB and Cc5 has $\delta^{13}C$ values between +0.8 and +1.6 ‰ VPDB and $\delta^{18}O$ ranging between -5.7 and -4.4 ‰ VPDB (Fig. 8A).

Calcite cement Cc6 to Cc8 show depleted $\delta^{18}O$ values with respect their adjacent host rocks (Fig. 8B). For Cc6, the $\delta^{13}C$ ranges between -8.9 and +3.7 ‰ VPDB and the $\delta^{18}O$ between -10.7 and -5.8 ‰ VPDB (Fig.8A). Cc7 has $\delta^{13}C$ values between -1.73 and -0.94 ‰ VPDB and $\delta^{18}O$ ranging between -11.3 and -9.58 ‰ VPDB (Fig. 8A). The $\delta^{13}C$ for Cc8 ranges between -0.3 and -0.2 ‰ VPDB and the $\delta^{18}O$ between -7.3 and -6.2 ‰ VPDB (Fig.8A).

4.5.3. Clumped isotopes thermometry

For this study, clumped isotopes thermometry has been applied to calcite cement Cc3 and Cc6. The results are presented in a $\delta^{18}O_{fluid}$ vs clumped temperature cross-plot (Fig. 9) and in Table 2. $\delta^{18}O_{fluid}$ in ‰ VSMOW of fluids are calculated from clumped temperatures using the equation of Friedman and O'Neil (1977).

For Cc3, the Δ_{47} is 0.579 ± 0.011 ‰, which translates into a temperature of 69.1 ± 5.3 ºC and a $\delta^{18}O_{fluid}$ of +5.4 ± 0.9 ‰ VSMOW. The analysed Δ_{47} for Cc6 is 0.579 ± 0.008 ‰, which translates into a temperature of 74.2 ± 4 ºC and a $\delta^{18}O_{fluid}$ of +5.1 ± 0.7 ‰ VSMOW.

4.5.4. Strontium isotopes

The Areny Formation limestone has an $^{87}Sr/^{86}Sr$ ratio of 0.707841 (Fig.9, Table S3). Only calcite cement Cc3, Cc5, and Cc6 could be sampled, obtaining $^{87}Sr/^{86}Sr$ ratios of 0.707922, 0.708230, and 0.707817, respectively (Fig.10, Table S3).

4.5.5. Elemental composition

The Fe, Mg, Sr, and Mn contents and Ca/Fe and Mg/Ca molar ratios of calcite cement Cc1, Cc3, Cc4, Cc5, and Cc6 are presented in table S4.

The elemental composition of calcite cement Cc1 shows values ranging from 172 to 1940 ppm in Fe and from 1096 to 6925 ppm in Mg, Sr, and Mn contents range from below the detection limit to 3592 and 361 ppm, respectively. Calcite cement Cc3 has values ranging from below the detection limit to 548 ppm in Fe and from 289 to 4169 ppm in Mg. The Sr and Mn contents range from below the detection limit to 879 and 477 ppm,

490 respectively. In calcite cement Cc4, the Fe content is below the detection limit, whereas
491 Mg shows values ranging from 801 to 4560 ppm. The Sr and Mn contents range from
492 below the detection limit to 275 and 384 ppm, respectively. For calcite cement Cc5, Mg
493 content ranges from 672 to 2765 ppm and the Fe, Sr and Mn contents range from below
494 the detection limit to 3028, 1851, and 365 ppm, respectively. The Mg content of calcite
495 cement Cc6 range from 679 to 4353 ppm whereas its Fe, Sr and Mn contents range from
496 below the detection limit to 3021, 656, and 362 ppm, respectively.

497 The elemental composition of cement Cc1, Cc3, Cc4, Cc5 and Cc6 shows a good Mg/Fe
498 and Mn/Fe correlation and a bad correlation with the Sr content. The distribution of the
499 Mg/Fe and Mn/Fe results shows two different fields (Fig. 11A and B). The first field (light
500 grey) includes calcite cement Cc1 and Cc3 and shows a wide range of Mg and Mn
501 content and narrow range of Fe content, whereas the second one (dark grey) includes
502 cement Cc5 and Cc6 and shows a wide range of Fe content and narrow range of Mg
503 and Mn content.

504 Although the elemental composition in natural carbonates does not always reflect
505 equilibrium partitioning (Reeder and Grams, 1987; Paquette and Reeder, 1995),
506 precipitation in equilibrium is assumed in this study to differentiate between different
507 types of fluids from which the studied calcites precipitated. Thus, molar ratios between
508 Ca and Fe, Sr, Mn and Mg were calculated for Cc1, Cc3, Cc4, Cc5, and Cc6 since their
509 values yield an estimation of the compositions of the former fluid (Table 3). Molar ratios
510 were calculated using the formula of McIntire (1963) and using K_{Mg}=0.097 at 70 ºC (Katz,
511 1973), K_{Fe}=5 at 25 ºC (Tucker and Wright, 1990), K_{Mn}=8 at 25º C (Lorens, 1981),
512 K_{Sr}=0.08 at 100ºC (Kinsman, 1969). The Ca/Fe molar ratio of cement Cc1, Cc3, Cc5 and
513 Cc6 ranges from 1390 to 15903, from 4963 to 19934, from 836 to 6993 and from 880 to
514 3912, respectively. The Mg/Ca molar ratio ranges from 0.047 to 0.304 for Cc1, from
515 0.069 to 0.18 for Cc3, from 0.034 to 0.197 for Cc4, from 0.03 to 0.121 for Cc5 and from
516 0.044 to 0.195 for Cc6. The Ca/Fe and Mg/Ca ratios are plotted in Fig. 11C. The Sr/Ca

molar ratios of cement Cc1, Cc3, Cc4, Cc5 and Cc6 range from 0.006 to 0.052, from 0.006 to 0.013, from 0.007 to 0.02, from 0.0052 to 0.027 and from 0.006 to 0.019, respectively. The Mn/Ca ratios range from 0.000032 to 0.000085 for Cc1, from 0.000032 to 0.00011 for Cc3, from 0.000033 to 0.000091 for Cc4, from 0.00025 to 0.000086 for Cc5 and from 0.000023 to 0.000083 for Cc6.

5. Discussion

5.1. Timing of fracture development

The sequence of fractures F1 to F7 documented in this work characterizes the evolution of deformation of the Lower Pedraforca thrust sheet.

The hydroplastic behaviour of F1 normal faults indicate that they were formed when the sediments were still poorly consolidated (Petit and Beauchamp,1986; Petit and Laville, 1987) and therefore, at shallow depths soon after deposition of the Upper Cretaceous Areny Formation and Middle Eocene syn-orogenic sediments. Similar fracture patterns also affecting the Areny Formation have been observed in other areas of the Lower Pedraforca thrust sheet (Soliva and Benedicto, 2004, 2005; Soliva et al., 2006, 2008) (Fig. 2A).

Fractures F2, F3, F4 and F6 have been dated using U-Pb geochronology of calcite cement Cc3, Cc4, Cc6 and Cc7. The obtained ages (from 47.9 ± 1.3 Ma to 42.3 ± 0.8 Ma) indicate that these fractures formed during the emplacement of the Lower Pedraforca thrust sheet during the Lutetian. Furthermore, crosscutting relationships between fractures and bedding allow differentiating stages of deformation during this emplacement. Thus, fracture systems F2 and F3 arranged parallel and perpendicular to bedding, respectively, probably formed at the same stage of deformation since they both contain calcite cement Cc3 (from 47.3 ± 1 Ma to 45.7 ± 1.9 Ma). These fracture systems formed during layer-parallel shortening, and are associated to the first stages of

compression in many fold and thrust belts (Casini et al., 2011; Tavani et al., 2015). Fracture systems F4, F5, and F6 have a constant orientation regardless of the beds dip, indicating that they formed during the main or late stages of folding, once strata were already tilted (Casini et al., 2011). Considering crosscutting relationships between the different types of calcite cement (Fig. 7), F4 containing Cc5 probably formed prior to F5 containing Cc6. Contrarily, F4 containing Cc6 and F5 formed at the same time since they contain the same type of calcite cement (from 47.2 ± 0.7 Ma to 45.1 ± 1.2 Ma). The presence in the thrust front of hydroplastic normal faults F1 with Cc6 and striae sets showing a reverse motion indicate that they were reactivated during this stage. This reactivation has also been observed in other areas of the Lower Pedraforca thrust sheet (Fig. 2A), where they show oblique and strike-slip striae sets (Soliva and Benedicto, 2004, 2005). F1 hydroplastic normal faults were reactivated probably to accommodate tilting and changes in the orientation during folding due to a tectonically-induced fluid pressure increase or because they represent a weak surface that facilitates reactivation (Letouzey et al., 1990; Sibson, 1995; Aydin, 2000; Wiprut and Zoback, 2000; Chi et al., 2012; Cobbold et al., 2013; Rutqvist et al., 2013; Soumaya et al., 2015; Wisseall et al., 2018). The presence of hydraulic breccias in thrust fault zones and normal faults tilted to low angles, or 0º, can be accounted for by a combination of both processes. U-Pb dates of 42.9 ± 0.9 Ma and 42.3 ± 0.8 Ma obtained for calcite cement Cc7 in fractures F6 reveal that these fractures formed after F4 and F5.

Normal faults F7 affect well-cemented Eocene-Oligocene conglomerates. Their NNW-SSE orientation is not consistent with the E-W trend of the main south Pyrenean structures (Vergés and Muñoz, 1990). The U-Pb age obtained for cement Cc8 precipitated in F7 (30.2 ± 2 Ma) suggests that their formation could be related to an E-W local extension affecting the Eocene-Oligocene conglomerates, which were deposited during the reactivation of the Lower Pedraforca thrust sheet (Vergés, 1993).

568 5.2. Evolution of the palaeohydrological system

569 The evolution of the palaeohydrological system through time within the Lower Pedraforca
570 thrust sheet is inferred from the geochemical data of calcite cement Cc1 to Cc8.

571 The $\delta^{13}C$ of most of the studied calcite cement is similar to their adjacent host rocks,
572 indicating a high interaction between fluids and host rocks (Fig. 8). This similarity is not
573 observed for Cc2 in locality G1, thus indicating the influence of soil-derived CO_2 or
574 oxidation of organic matter within the host rocks (Irwin et al., 1977; Cerling et al., 1989).
575 In the same locality, cement Cc6 postdating Cc2 is also in disequilibrium with their
576 adjacent host rock whereas it has similar $\delta^{13}C$ to that of Cc2 (Fig. 8). This could indicate
577 that the $\delta^{13}C$ of fluids from which Cc6 precipitated locally reequilibrated with Cc2 instead
578 of with the host carbonates. The $\delta^{13}C$ and $\delta^{18}O$ of Cc2 suggest that this cement probably
579 precipitated from meteoric waters (Veizer and Hoefs, 1976) (Fig. 8).

580 Regarding to the $\delta^{18}O$, values for calcite cement Cc1 to Cc5 are similar to their host
581 carbonates (Fig. 8). This could indicate a relatively closed palaeohydrological system, in
582 which fluid-host rock interaction was high enough to equilibrate the $\delta^{18}O$ of the host
583 carbonates with that of the fluid (Banner and Hanson, 1990) but not high enough to
584 modify the $\delta^{13}C$ signature of the host rock, as evidenced by the wide spread of values
585 for each cement (Fig. 8). This different behaviour of the $\delta^{18}O$ and $\delta^{13}C$ may be related to
586 the different concentrations of these isotopic species in the host rock, which require
587 different fluid/rock ratios to be reequilibrated with fluids (Banner and Hanson, 1990). For
588 calcite cement Cc6, Cc7 and Cc8, however, the $\delta^{18}O$ is progressively more depleted with
589 respect to their adjacent host carbonates, suggesting an opening of the
590 palaeohydrological system or higher temperature conditions during calcite precipitation
591 (Fig. 8). In this setting, and in opposition with that for Cc1 to Cc5 calcite cement, fluid-
592 host rock interaction was not sufficient to re-equilibrate the $\delta^{18}O$ of host rocks with that
593 of fluids due to a lower water/host rock ratio. The opening of the palaeohydrological

system could have been favoured by the development of fractures F4 to F7, which have a major length and width than that of F2 and F3. The development of longer and wider fractures increased the reservoir permeability and facilitated the opening of the system to external fluids and the decrease the water/host interaction (Travé et al., 2000; Hurai et al., 2015; Muñoz-López et al., 2020). The depletion in $\delta^{18}O$ of Cc6, Cc7, and Cc8 with respect to their host rocks could be due to the input of hotter fluids or mixing between formation and more diluted meteoric waters (Zheng and Hoefs, 1993; Travé et al., 1997; Immenhauser et al., 2007; Breesch et al., 2009; Vilasi, 2010; Vandeginste et al., 2012; Beaudoin et al., 2014; Lacroix et al., 2014; Cruset et al., 2016; 2018; Nardini et al., 2019). The presence of oil seeps trapped within Cc6 precipitated in F4 fractures also evidences an open fluid system. The origin of these hydrocarbons is unclear since the main source rock in the SE Pyrenees is the Armàncies Formation (Caja et al., 2006). This unit consists of lower Eocene carbonates in the footwall of the Lower Pedraforca thrust sheet below its main Upper Triassic detachment (Fig. 1C). However, in the western continuation of the Lower Pedraforca thrust sheet, the Montsec and Serres Marginals thrust units, Early Jurassic source rocks have been identified (Martínez-del Olmo, 2019). Therefore, a possible Jurassic origin for oil in the Lower Pedraforca thrust sheet cannot be ruled out. The low $\delta^{13}C$ value measured in one sample of Lower Jurassic limestones from locality G2 (-6.06 ‰ VPDB) could account for organic matter oxidation (Irwin et al., 1977). Contrarily, the $\delta^{13}C$ of the other measured Jurassic host rocks are within the range of Jurassic-Cretaceous marine carbonates (Veizer et al., 1999) (Fig. 8). In this scenario, F4 fractures, where Cc6 precipitated, may have facilitated interconnection between different hydrostratigraphic units and the migration of hydrocarbons to shallower areas.

The two fields observed in the Mn/Fe cross-plot (Fig. 11B) also indicate the behaviour of the palaeohydrological system during fluid migration within the Lower Pedraforca thrust sheet. Thus, as the distribution coefficient of Mn (K_{Mn}) is higher than the distribution coefficient of Fe (K_{Fe}), in a closed palaeohydrological system, the Mn content decreases

faster than the Fe content in the fluid as calcite precipitates (Dromgoole and Walter, 1990). In contrast, if Fe content decreases faster than that of Mn during calcite precipitation, it will necessarily imply an open system. In the Lower Pedraforca thrust sheet, calcite cement Cc1 and Cc3 fall in the field with a faster decrease in Mn than in Fe (Fig. 11B), and thus, reflecting a relatively closed system and high fluid-rock interaction. Contrarily, cement Cc5 and Cc6 fall in the field with a faster Fe decrease than Mn and therefore, that they precipitated in a more open palaeohydrological fluid system in which fluid-rock interaction was low.

The elemental composition of the calcite cement also records the composition of fluids migrating within the Lower Pedraforca thrust sheet. The Mn/Ca and Sr/Ca molar ratios of fluids from which calcite cement Cc1, Cc3, Cc4, Cc5 and Cc6 precipitated range from 0.000231 to 0.000091 for Mn/Ca and from 0.0052 to 0.0522 for Sr/Ca. These values are similar to those of calcites precipitated from formation waters (McIntire, 1963; Howson et al., 1987; Tucker and Wright, 1990). The Mg/Ca and Ca/Fe ratios of calcite cement Cc1 and Cc3 (from 0.03 to 0.304 for Mg/Ca and from 1390 to 19934 for Ca/Fe) indicate the influence of marine, formation and meteoric waters (Tucker and Wright, 1990; Kolker and Chou, 1994; Steuber and Rauch, 2005; Ligi et al., 2013) (Fig. 11C), whereas in calcite cement Cc4, Cc5 and Cc6 (from 0.03 to 0.197 for Mg/Ca and from 836 to 6993 for Ca/Fe) these ratios suggest the presence of meteoric and formation waters (Howson et al., 1987; Tucker and Wright, 1990; Kolker and Chou, 1994). These results suggest that during the evolution of the fluid system, the influence of marine waters is stronger during the precipitation of cement Cc1 and Cc3, when the fluid system was relatively closed (Fig. 11C). In contrast, during the precipitation of calcite cement Cc5 and Cc6, the influence of meteoric waters was stronger, suggesting the opening of the fluid system to these fluids (Fig. 11C).

The $^{87}Sr/^{86}Sr$ ratios of calcite cement Cc3 (0.707922) and Cc5 (0.708230) are higher than expected for cement precipitated from Middle Eocene seawater (McArthur et al.,

2001) and thus, fluids had to interact with a more radiogenic source. The $^{87}Sr/^{86}Sr$ ratio of Cc3 falls within the range of the Upper Triassic evaporites from Keuper facies (Fig. 10), indicating that fluids from which this cement precipitated probably interacted with these evaporites. An alternative interpretation would imply fluids interacting with clay minerals such as illite and/or smectite (Katz and Bullen, 1996), indicated by the $^{87}Sr/^{86}Sr$ ratio of Cc5 higher than Upper Triassic evaporites (Fig. 10). The source of these minerals could be the Garumnian continental deposits. On the other hand, calcite cement Cc6 shows the lowest $^{87}Sr/^{86}Sr$ ratio (0.707817, Fig. 10), which could indicate the influence of either middle Eocene seawater or of brines from the Upper Triassic Keuper facies, which act as a detachment of the thrust system. The absence in Cc6 of any marine influence in the Ca/Fe and Mg/Ca ratios (Fig. 11C), together with its $\delta^{18}O_{fluid}$ of +5.1 ± 0.7 ‰ may support the influence of Upper Triassic evaporites rather than middle Eocene seawater.

5.3. Relationships between deformation style and fluid flow

A conceptual model divided in five stages showing the relationships between fluid flow and fracturing during the development of the Lower Pedraforca thrust sheet is presented (Fig. 12).

During the first stage (T1, Fig. 3 and 12A), hydroplastic normal faults F1 formed soon after the deposition of the Upper Cretaceous Areny Formation at shallow conditions. During this event, there was no cement precipitation within faults, probably because faulting occurred in poorly consolidated sediments with internal heterogeneities that act as zones of low permeability (Caine and Minor, 2009; Loveless et al., 2011), or because the fluid that migrated along fractures was undersaturated with respect to calcite.

During T2 (Fig. 12B), Cc1 and Cc2 precipitated in the intergranular, moldic and vug porosities within the Jurassic Bonansa and Upper Cretaceous Areny Formations and the Palaeocene Garumnian facies. Cc1 and Cc2 probably precipitated from formation and

674 meteoric waters, respectively. These two types of cement precipitated before the
675 Lutetian shortening event related to the emplacement of the Lower Pedraforca thrust
676 sheet, as evidenced by crosscutting relationships between these types of cement and
677 cement Cc3 (Fig. 6A and B and 7). Therefore, they probably precipitated during burial
678 diagenesis of the Jurassic, Upper Cretaceous, and Palaeocene sediments. During this
679 burial stage, bed-parallel stylolites St1 formed in carbonate rocks of the Bonansa and
680 Areny Formations and Garumnian facies.

681 The Lower Pedraforca thrust sheet was emplaced during the Lutetian (stages T3 and
682 T4). At stage T3, fractures F2 and F3 formed during layer-parallel shortening, and calcite
683 cement Cc3 and Cc4 precipitated post-dating stylolites St1 (Fig. 3 and 12C). During this
684 period, formation waters, possibly derived from Upper Triassic evaporites and in isotopic
685 equilibrium with adjacent Upper Cretaceous and Palaeocene host rocks, migrated along
686 fractures in a closed system. The precipitation temperature of ~70 ºC obtained for Cc3
687 is higher than expected by burial in the frontalmost part of the Lower Pedraforca thrust
688 sheet, where the complete pile of sediments is less than 500 m (Vergés, 1993).
689 Considering a linear geothermal gradient of 30 ºC, which is slightly high for foreland
690 basins, the estimated burial depth is ~2.3 km. This thermal gradient was tested in the
691 southern Pyrenean foreland basins by Vergés et al. (1998). This depth is consistent with
692 the stratigraphic thickness of the northern imbricated Lower Pedraforca thrust sheet (Fig.
693 1C; Vergés 1993), fact that could indicate that formation waters migrated from the deeper
694 parts of the thrust sheet to the shallow thrust front along F2 and F3 fractures. Rapid fluid
695 flow would account for thermal disequilibrium with their adjacent host rocks (Bons et al.,
696 2012; Beaudoin et al., 2014). During T3, fractures F3 cut hydroplastic normal faults F1
697 in the Upper Cretaceous Areny Formation. In the thrust front, however, hydroplastic
698 normal faults developed within middle Eocene syn-orogenic sediments in Q. These faults
699 were reactivated during progressive tilting of bedding and Cc4 precipitated. The
700 dispersion in $\delta^{18}O$ of this cement (from -6.9 to -2.6 ‰ VPDB) could indicate different

precipitation temperatures, probably related to different burial conditions during the progressive deposition of the syn-orogenic sediments.

The fourth stage (T4) is related to folding and thrusting when F4 reverse and F5 strike-slip faults and F6 veins formed (T4, Fig. 3 and 12D). During this event, recorded by cement Cc5, Cc6, and Cc7, the fluid system opened to formation waters carrying hydrocarbons (Fig. 8, 10 and 11C). These fluids probably interacted with Upper Triassic evaporites as indicated by the $^{87}Sr/^{86}Sr$ ratio of Cc6 (0.707817). This new input of formation waters was coupled with a progressive decrease of the water/host rock interaction, resulting in the precipitation of calcite cement Cc6 and Cc7, with $\delta^{18}O$ depleted with respect to their adjacent host rocks (Fig. 8). The temperature about 74 ºC obtained for Cc6 is also higher than expected by burial. Considering the geothermal gradient of 30 ºC, an estimated burial depth of ~2.4 km is obtained, which is consistent with the stratigraphic thickness of the northern imbricate Lower Pedraforca thrust sheet (Fig. 1C; Vergés 1993). The increase of temperature of Cc6 with respect to Cc3 could indicate an increase of burial during deposition of the Bellmunt Formation conglomerates, which buried the Lower Pedraforca thrust sheet during the Lutetian (Burbank et al., 1992a). As deformation progressed, St1 stylolites were passively rotated in the fold limbs and St2 stylolites postdating Cc6 formed parallel and orthogonal to F4 and F5 fractures. St2 formed due to shortening during the emplacement of the Lower Pedraforca imbricates. The preferential development of these stylolites in close relationship with F4 and F5 accounts for this scenario. During progressive folding, F1 hydroplastic normal faults in the Upper Cretaceous Areny Formation were reactivated as reverse faults in the thrust front, whereas in the central area of the Lower Pedraforca thrust sheet (Fig. 2A), they were reactivated as strike-slip faults, allowing fluid migration (Soliva and Benedicto, 2004, 2005; Soliva et al., 2006, 2008). Such reactivations increased the fracture reservoir heterogeneity and are interpreted to have been induced by fluid pressure build-up and/or reorientation of pre-existing fractures during folding, as

728 reported in other fractured reservoirs worldwide (Letouzey et al., 1990; Sibson, 1995;
729 Aydin, 2000; Wiprut and Zoback, 2000; Roure et al., 2005; Chi et al., 2012; Cobbold et
730 al., 2013; Rutqvist et al., 2013; Soumaya et al., 2015; Wisseall et al., 2018). Fluids
731 migrated along discrete fault planes or through hydraulic fracturing triggered by fluid
732 overpressures in the footwall of thrusts displaced along Upper Triassic evaporites.
733 According to Aydin (2000) in the Uinta basin (United states), hydraulic fractures act as
734 preferential paths for fluids in areas with low permeability.

735 Finally, during the reactivation of the thrust system (T5, Fig. 3 and 12E) at the Oligocene,
736 normal faults F7 formed and fluids also in disequilibrium with their adjacent host rocks
737 migrated through fractures precipitating cement Cc8 in a relatively open system.

738 ### 5.4. Pyrenees fluid flow comparison to other fold and thrust belts examples

739 The Lower Pedraforca corresponds to a single thrust sheet and its emplacement
740 represents a short period of time of the whole south Pyrenean foreland basin evolution
741 under marine conditions (Vergés et al., 1995). Despite these limited area and time
742 scales, the fluid flow behaviour in the Lower Pedraforca thrust sheet is similar to that of
743 in other Pyrenean transects as well as in larger scale fold and thrust belts (Fig. 13). In all
744 cases, fluid-related processes are controlled by the evolution of deformation patterns,
745 from layer-parallel shortening (Fig. 13A) to subsequent folding and thrusting (Fig. 13B).
746 The Puig-reig anticline, in the south Pyrenean foreland basin, is located to the south of
747 the frontal thrust and thus corresponding to a younger foreland region than that of the
748 Lower Pedraforca thrust sheet. In this anticline, hydrothermal fluids migrated through
749 early stratabound strike-slip faults and low angle thrusts. Subsequently, during folding
750 and crestal graben development, the palaeohydrological system opened to the input of
751 meteoric waters that mixed at depth with the hydrothermal fluids (Cruset et al., 2016). A
752 similar opening of the fluid system through time is observed in other south Pyrenean
753 structures developed at different periods of time and at different foreland domains than

754 the Lower Pedraforca thrust sheet, such as the Vallfogona, l'Escala, l'Abocador, Larra-
755 Eaux-Chaudes and Jaca thrusts (Lacroix et al., 2014; Crognier et al., 2018; Cruset et al.,
756 2018). Elsewhere, in larger fold and thrust belts such as the Bighorn Basin in the Sevier
757 thrust belt and in the Ionian fold belt of Albania, a closed palaeohydrological system
758 prevailed during layer-parallel shortening, which opened to external fluids during
759 fracturing associated to folding and thrusting (Vilasi et al., 2006; Beaudoin et al., 2013).
760 Likewise, in the Mexican fold and thrust belt and in the central Appalachians, fluids were
761 stratigraphically segregated during the early deformation, whereas the fluid system
762 became interconnected during fold tightening (Ferket et al., 2000, 2003; Lefticariu et al.,
763 2005; Fischer et al., 2009; Fitz-Diaz et al., 2011; Evans et al., 2012). In the Northern
764 Oman Mountains, pre-burial fluids migrated through fractures in a rock-buffered system,
765 and deep-sourced fluids migrated through thrust faults during the main stage of
766 compression (Breesch et al., 2009). In this example of fold belt from Oman, main thrust
767 faults acted as barriers for transversal fluid flow, since evidence of migration of fluids
768 were not observed in the hangingwall carbonates. Finally, the anticlines from the
769 Lurestan Province of Iran, in the Zagros fold belt, show a fracture pattern similar to that
770 observed in the Lower Pedraforca thrust sheet, although the Iranian folds are located in
771 a more external domain of the foreland basin. In this area, syn-sedimentary normal faults
772 were passively rotated into the anticline limbs during the main and later stages of folding
773 and were reactivated as reverse faults, where calcite cement containing hydrocarbons
774 precipitated (Casini et al., 2011; 2018). Like in the Lower Pedraforca thrust sheet, the
775 presence of hydrocarbons within fracture-filling calcites indicates the opening of the fluid
776 system during this main stage of folding and the input of exotic fluids in contact with
777 petroleum source rocks.

778 The changes of the fluid regime in compressional settings are also observed in
779 extensional regimes such as the Neogene Vallès-Penedès (Baqués et al., 2010;
780 Cantarero et al., 2014) and the Corinth rift (Benedicto et al., 2008) extensional systems.

781 In these examples, during the first stages of upward propagation of normal faults, the
782 palaeohydrological system was relatively closed with high fluid-rock interaction, whereas
783 during the final stages of normal faulting it changed to a more open one, with lower fluid-
784 rock interaction.

785 6. Conclusions

786 The integration of field-based and petrographic observations, together with geochemical
787 and geochronological data allowed to differentiate up to eight types of calcite cement
788 (Cc1 to Cc8) and two sets of stylolites (St1 and St2) revealing the evolution of the
789 palaeohydrological system during the emplacement of the Lower Pedraforca thrust
790 sheet.

791 Relationships between calcite cement and fractures indicate that during hydroplastic
792 deformation related to the pre-shortening stage within the Lower Pedraforca thrust sheet,
793 there was no precipitation of calcite cement in fractures. During the progressive burial,
794 calcite cement Cc1 and Cc2 precipitated from formation waters in isotopic equilibrium
795 with their adjacent host rocks. Burial was also responsible for development of the bed-
796 parallel stylolites St1.

797 During middle Eocene (Lutetian) layer-parallel shortening, calcite cement Cc3 and Cc4
798 precipitated from fluids in a relatively closed palaeohydrological system with high fluid-
799 host rock interaction. Clumped isotopes thermometry indicates that calcite cement Cc3
800 precipitated from formation waters (~+5.4 ‰ VSMOW) at temperatures around 70 ºC.
801 This temperature, together with an $^{87}Sr/^{86}Sr$ ratio of 0.707922, indicates that formation
802 waters migrated forwards from the deeper domains in the Lower Pedraforca thrust sheet
803 to the shallower thrust front and probably interacting with Upper Triassic evaporites at
804 the base of the hangingwall succession. The $\delta^{18}O$ dispersion up to 4 ‰ VPDB of calcite
805 cement Cc4 could indicate different precipitation temperatures during the progressive
806 burial of syn-orogenic sediments deposited in the thrust front (Emery, 1987).

807 Progressive folding and thrusting, during Lutetian age, was coupled with tilting of St1
808 stylolites and precipitation of calcite cement Cc5 to Cc7. Clumped isotopes thermometry
809 indicates that Cc6 cement precipitated from formation waters (~+5 ‰ VSMOW) at
810 temperatures around 75 ºC, which are also interpreted as migrated from the deeper
811 regions of the thrust sheet to the thrust front. The $\delta^{18}O$ depletion of calcite cement Cc6
812 and Cc7 with respect to their adjacent host rocks and the presence of hydrocarbons in
813 Cc6 indicate an opening of the palaeohydrological system. The $^{87}Sr/^{86}Sr$ ratios of Cc5
814 (0.708230) and Cc6 (0.707817) suggests the influence of clay minerals, probably from
815 the Garumnian continental deposits, and of Upper Triassic evaporites, respectively.
816 During this period, stylolites St2 formed and previous hydroplastic fractures were
817 reactivated as reverse and strike-slip faults facilitating fluid flow. Cc7, precipitated after
818 Cc6 according to U-Pb geochronology, also precipitated from fluids in isotopic
819 disequilibrium with their adjacent host rocks.

820 Finally, large-scale folding of the Lower Pedraforca thrust sheet due to the emplacement
821 of younger thrust sheets below, induced the reactivation of its basal thrust during the
822 Oligocene. During this period, fluids in isotopic disequilibrium with their adjacent host
823 rocks migrated through local normal faults that cut Oligocene conglomerates in the
824 footwall of the Lower Pedraforca basal thrust and Cc8 precipitated.

825 The progressive shortening and concomitant fracturing and fluid flow in the Lower
826 Pedraforca thrust sheet share a common fluid evolution with other fold and thrust belt
827 domains in the Pyrenees as well as elsewhere alike the Sevier, Appalachians, Bighorn
828 basin, Ionian, Mexican, Zagros, and Oman fold and thrust belts

829 ## Acknowledgments

830 The isotopic and electron microprobe analyses were carried out at “Centres Científics i
831 Tecnològics” of the Universitat de Barcelona. Strontium analyses were done at the “CAI
832 de Geocronología y Geoquímica Isotópica (UCM-CEI)” of the Universidad Complutense

833 de Madrid. U-Pb geochronology was accomplished at FIERCE (Frankfurt Isotope and
834 Element Research Center, Goethe University). This is FIERCE contribution No. 20. The
835 clumped isotopes analyses were performed in the Qatar Stable Isotope Laboratory of
836 Imperial College of London. This research was performed within the framework of
837 DGICYT Spanish Project PGC2018-093903-B-C22 Ministerio de Ciencia, Innovación y
838 Universidades/Agencia Estatal de Investigación/Fondo Europeo de Desarrollo Regional,
839 Unión Europea, Alpimed (PIE-CSIC-201530E082), Subtetis project (PIE-CSIC-
840 201830E039), and Grup Consolidats de Recerca ”Geologia Sedimentària” (2017SGR-
841 824) and “Geodinàmica Interna” (2017SGR–847). The accurate and constructive
842 comments from Guilhem Hoareau, an anonymous reviewer and the editor Nicolas
843 Beaudoin helped to improve the original manuscript.

844 **References**

845 Aydin, A., 2000. Fractures, faults, and hydrocarbon entrapment, migration and
846 flow. Marine and Petroleum Geology 17, 797-814.

847 Banner, J.L., Hanson, G.N., 1990. Calculation of simultaneous isotopic and trace
848 element variations during water-rock interaction with applications to carbonate
849 diagenesis. Geochimia et Cosmochimica Acta 54, 3123-3137.

850 Baqués, V., Travé, A., Benedicto, A., Labaume, P., Cantarero, I., 2010.
851 Relationships between carbonate fault rocks and fluid flow regime during propagation of
852 the Neogene extensional faults of the Penedès basin (Catalan Coastal Ranges, NE
853 Spain). Journal of Geochemical Exploration 106, 24-33.

854 Beaudoin, N., Bellahsen, N., Lacombe, O., Emmanuel, L., Pironon, J., 2014.
855 Crustal-scale fluid flow during the tectonic evolution of the Bighorn Basin (Wyoming,
856 USA). Basin Research 26, 403-435.

857 Beaudoin, N., Huyghe, D., Bellahsen, N., Lacombe, O., Emmanuel, L.,
858 Mouthereau, F., Ouanhnon, L., 2015. Fluid systems and fracture development during

859 syn-depositional fold growth: An example from the Pico del Aguila anticline, Sierras
860 Exteriores, southern Pyrenees, Spain. Journal of Structural Geology 70, 23-38.
861 Beaudoin, N., Lacombe, O., Bellahsen, N., Emmanuel, L., 2013. Contribution of
862 Studies of Sub-Seismic Fracture Populations to Paleo-Hydrological Reconstructions
863 (Bighorn Basin, USA). Procedia Earth and Planetary Science 7, 57-60.
864 Benedicto, A., Plagnes, V., Vergély, P., Flotté, N., Schultz, R.A., 2008. Fault and
865 fluid interaction in a rifted margin: integrated study of calcite-sealed fault-related
866 structures (southern Corinth margin). Geological Society, London, Special Publications
867 299, 257-275.
868 Bons, P.D., Elburg, M.A. and Gómez-Rivas, E., 2012. A review of the formation
869 of tectonic veins and their microstructures. Journal of Structural Geology, 43, 33-62.
870 Breesch, L., Swennen, R., Vincent, B., 2009. Fluid flow reconstruction in hanging
871 and footwall carbonates: Compartmentalization by Cenozoic reverse faulting in the
872 Northern Oman Mountains (UAE). Marine and Petroleum Geology 26, 113-128.
873 Burbank, D.W., Puigdefàbregas, C., Muñoz, J.A., 1992a. The chronology of the
874 Eocene tectonic and stratigraphic development of the Eastern Pyrenean Foreland Basin.
875 NE Spain. Geol. Soc. America Bull. 104, 1101-1120.
876 Burbank, D.W., Vergés, J., Muñoz, J.A., Bentham, P., 1992b. Coeval hinward-
877 and forward-imbricating thrusting in the south-central Pyrenees, Spain: Timing and rates
878 of shortening and deposition. Geological Society of America Bulletin 104, 3-17.
879 Burisch, M. et al., 2017. Methane and the origin of five-element veins: Mineralogy,
880 age, fluid inclusion chemistry and ore forming processes in the Odenwald, SW Germany.
881 Ore Geology Reviews, 81, 42-61.
882 Caine, J.S., Minor, S.A., 2009. Structural and geochemical characteristics of
883 faulted sediments and infewrences on the role of water in deformation, Rio Grande Rift,
884 New Mexico. GSA Bulletin 121, 1325-1340.

885 Calvet, F., Porta, N.S.d., Salvany, J.M., 1993. Cronoestratigrafía (Palinología) del
886 Triásico Sudpirenaico y del Pirineo Vasco-Cantábrico. Acta Geologica Hispanica 28, 33-
887 48.Caja, M.A., Permanyer, A., Marfil, R., Al-Asm, I.S. and Martín-Crespo, T., 2006. Fluid
888 flow record from fracture-fill calcite in the Eocene limestones from the South-Pyrenean
889 Basin (NE Spain) and its relationship to oil shows. Journal of Geochemical Exploration,
890 89, 27-32.
891 Cantarero, I., Alías, G., Cruset, D., Carola, E., Lanari, P., Travé, A., 2018. Fluid
892 composition changes in crystalline basement rocks from ductile to brittle regimes. Global
893 and Planetary Change 171, 273-292.
894 Cantarero, I., Travé, A., Alías, G., Baqués, V., 2014. Polyphasic hydrothermal
895 and meteoric fluid regimes during the growth of a segmented fault involving crystalline
896 and carbonate rocks (Barcelona Plain, NE Spain). Geofluids 14, 20-44.
897 Casini, G., Gillespie, P.A., Vergés, J., Romaire, I., Fernández, N., Casciello, E.,
898 Saura, E., Mehl, C., Homke, S., Embry, J.-C., Aghajari, L., Hunt, D.W., 2011. Sub-
899 seismic fractures in Foreland fold and Thrust belts: insight from the Lurestan Province,
900 Zagros Mountains, Iran. Petroleum Geoscience 17, 263-282.
901 Casini, G., Romaire, I., Casciello, E., Saura, E., Vergés, J., Fernández, N., Hunt,
902 D.W., 2018. Fracture characterization in sigmoidal folds: Insights from the Siah Kuh
903 anticline, Zagros, Iran. AAPG Bulletin 102, 369-399.
904 Cerling, T.E., Quade, J., Wang, Y. and Bowman, J.R., 1989. Carbon isotopes in
905 soils and palaeosols as ecology and palaeoecology indicators. Nature, 341, 138-139.
906 Chi, G., Xue, C., Qing, H., Xue, W., Zhang, J., Sun, Y., 2012. Hydrodynamic
907 analysis of clastic injection and hydraulic fracturing structures in the Jinding Zn-Pb
908 deposit, Yunnan, China. Geoscience Frontiers 3, 73-84.
909 Choukroune, P., team, E., 1989. The ECORS Pyrenean deep seismic profile
910 reflection data and the overall structure of an orogenic belt. Tectonics 8, 23-39.

911 Claypool, G.E., Kaplan, W.T., Kaplan, I.R., Sakai, H., Zak, I., 1980. The age
912 curves of sulfur and oxygen isotopes in marine sulfate and their mutual interpretations.
913 Chemical Geology 28, 199-260.
914 Cobbold, P.R., Zanella, A., Rodrigues, N., Løseth, H., 2013. Bedding-parallel
915 fibrous veins (beef and cone-in-cone): Worldwide occurrence and possible significance
916 in terms of fluid overpressure, hydrocarbon generation and mineralization. Marine and
917 Petroleum Geology 43, 1-20.
918 Craig, H., Gordon, I.-I., 1965. Deuterium and oxygen-18 variations in the ocean
919 and the marine atmosphere, in: Tongiorgi, E. (Ed.), Proceedings of a Conference on
920 Stable Isotopes in Oceanographic Studies and Paleotemperatures. Consiglio Nazionale
921 delle Richerche, Laboratorio di Geologia Nucleare, Pisa, Italy, pp. 9-130.
922 Crognier, N., Hoareau, G., Aubourg, C., Dubois, M., Lacroix, B., Branellec, M.,
923 Callot, J.P., Vennemann, T., 2018. Syn-orogenic fluid flow in the Jaca basin (south
924 Pyrenean fold and thrust belt) from fracture and vein analyses. Basin Research, 1-30.
925 Cruset, D., Cantarero, I., Travé, A., Vergés, J., John, C.M., 2016. Crestal graben
926 fluid evolution during growth of the Puig-reig anticline (South Pyrenean fold and thrust
927 belt). Journal of Geodynamics 101, 30-50.
928 Cruset, D., Cantarero, I., Vergés, J., John, C.M., Muñoz-López, D., Travé, A.,
929 2018. Changes in fluid regime in syn-orogenic sediments during the growth of the south
930 Pyrenean fold and thrust belt. Global and Planetary Change 171, 207-224.
931 Davies, A.J., John, C.M., 2019. The clumped ($^{13}C^{18}O$) isotope composition of
932 echinoid calcite: Further evidence for “vital effects” in the clumped isotope proxy.
933 Geochimica et Cosmochimica Acta 245, 172-189.
934 Delvaux, D., Sperner, B., 2003. New aspects of tectonic stress inversion with
935 reference to the TENSOR program, in: Nieuwland, D.A. (Ed.), New Insights into
936 Structural Interpretation and Modelling. Geological Society, London, Special
937 Publications, pp. 75-100.

938 Dennis, K.J., Affeck, H.P., Passey, B.H., Schrag, D.P., Eiler, J.M., 2011. Defining
939 an absolute reference frame for ‘clumped’ isotope studies of CO2. Geochimia et
940 Cosmochimica Acta 75, 7117-7131.
941 Dimmen, V., Rotevatn, A., Peacock, D.C.P., Nixon, C.W., Naerland, K., 2017.
942 Quantifying structural controls on fluid flow: Insights from carbonate hosted fault damage
943 zones on the Maltese Islands. Journal of Structural Geology 101, 43-57.
944 Dromgoole, E.L., Walter, L.M., 1990. Iron and manganese incorporation into
945 calcite: effects of growth kinetics, temperature, and solution chemistry. Chemical
946 Geology 81, 311-336.
947 Egholm, D.L., Clausen, R.O., Sandiford, M., Kristensen, M.B., Korstgård, J.A.,
948 2008. The mechanics of clay smearing along faults. Geology 36, 787-790.
949 Emery, D., 1987. Trace-element source and mobility during limestone burial
950 diagenesis, an example from the Middle Jurassic of eastern England. Geological Society,
951 London, Special Publications, 36(1), 201-217.
952 Evans, M.A., Bebeout, G.E., Brown, C.H., 2012. Changing fluid conditions during
953 folding: An example from the central Appalachians. Tectonophysics 576-577, 99-115.
954 Ferket, H., Roure, F., Swennen, R. and Ortuño, S., 2000. Fluid migration placed
955 into the deformation history of fold-and-thrust belts: an example from the Veracruz basin
956 (Mexico). Journal of Geochemical Exploration, 69-70, 275-279.
957 Ferket, H., Swennen, R., Ortuño, S. and Roure, F., 2003. Reconstruction of the
958 fluid flow history during Laramide foreland fold and thrust belt development in eastern
959 Mexico: cathodoluminescence and $\delta^{18}O$-$\delta^{13}C$ isotope trends of calcite-cemented
960 fractures. Journal of Geochemical Exploration, 78-79, 163-167.
961 Fischer, M.P., Higuera-Díaz, I.C., Evans, M.A., Perry, E.C., Lefticariu, L., 2009.
962 Fracture-controlled paleohydrology in a map-scale detachment fold: Insights from the
963 analysis of fluid inclusions in calcite and quartz veins. Journal of Structural Geology 31,
964 1490-1510.

965 Fitz-Diaz, E., Hudleston, P., Siebenaller, L., Kirschner, D., Camprubí, A., Tolson,
966 G., Puig, T.P., 2011. Insights into fluid flow and water-rock interaction during deformation
967 of carbonate sequences in the Mexican fold-thrust belt. Journal of Structural Geology 33,
968 1237-1253.
969 Friedman, I., O'Neil, J.R., 1977. Compilation of stable isotope fractionation factors
970 of geochemical interest, in: Fleischer, M. (Ed.), Data of Geochemistry, U. S. Gov. Print.
971 Off. Washington D. C., pp. 1-12.
972 Gerdes, A. and Zeh, A., 2006. Combined U–Pb and Hf isotope LA-(MC-)ICP-MS
973 analyses of detrital zircons: Comparison with SHRIMP and new constraints for the
974 provenance and age of an Armorican metasediment in Central Germany. Earth and
975 Planetary Science Letters, 249, 47-61.
976 Gerdes, A. and Zeh, A., 2009. Zircon formation versus zircon alteration — New
977 insights from combined U–Pb and Lu–Hf in-situ LA-ICP-MS analyses, and
978 consequences for the interpretation of Archean zircon from the Central Zone of the
979 Limpopo Belt: Chemical Geology. Chemical Geology, 261(3-4), 230-243.
980 Grool, A.R. et al., 2018. Insights Into the Crustal-Scale Dynamics of a Doubly
981 Vergent Orogen From a Quantitative Analysis of Its Forelands: A Case Study of the
982 Eastern Pyrenees. Tectonics, 37(2), 450-476.
983 Guo, W., Mosenfelder, J.L., Goddard, W.A., Eiler, J.M., 2009. Isotopic
984 fractionations associated with phosphoric acid digestion of carbonate minerals: Insights
985 from first-principles theoretical modeling and clumped isotope measurements.
986 Geochimia et Cosmochimica Acta 73, 7203-7225.
987 Gutmanis, J., Oró, L.A.i., Díez-Canseco, D., Chebbihi, L., Awdal, A., Cook, A.,
988 2017. Fracture analysis of outcrop analogues to support modelling of the subseismic
989 domain in carbonate reservoirs, south-central Pyrenees, in: Ashton, M., Dee, S.J.,
990 Wennberg, O.P. (Eds.), Subseismic-Scale Reservoir Deformation. Geological Society,
991 London, Special Publications, pp. 139-156.

992 Howson, M.R., Pethybridge, A.D., House, W.A., 1987. Synthesis and distribution
993 coefficients of low-magnesium calcites. Chemical Geology 64, 79-87.
994 Huntington, K.W., Eiler, J.M., Affeck, H.P., Guo, W., Bonifacie, M., Yeung, L.Y.,
995 Thiagarajan, N., Passey, B., Tripati, A., Daëron, M., Came, R., 2009. Methods and
996 limitations of 'clumped' CO2 isotope (Δ47) analysis by gas-source isotope ratio mass
997 spectrometry. Journal of Mass Spectrometry 44, 1318-1329.
998 Hurai, V., Huraiová, M., Slobodník, M. and Thomas, R., 2015. Chapter 9 - Stable
999 Isotope Geochemistry of Geofluids. In: V. Hurai, M. Huraiová, M. Slobodník and R.
1000 Thomas (Eds.), Geofluids. Elsevier, pp. 293-344.
1001 Immenhauser, A., Dublyansky, Y.V., Verwer, K., Fleitman, D., Pashenko, S.E.,
1002 2007. Textural, elemental and isotopic characteristics of Pleistocene phreatic cave
1003 deposits (Jabal Madar, Oman). Journal of Sedimentary Research 77, 68-88.
1004 Irwin, H., Curtis, C. and Coleman, M., 1977. Isotopic evidence for source of
1005 diagenetic carbonates formed during burial of organic-rich sediments. Nature, 269, 209-
1006 213.
1007 John, C.M., Bowen, D., 2016. Community software for challenging isotope
1008 analysis: First applications of "Easotope" to clumped isotopes. Rapid Communications
1009 in Mass Spectrometry 30, 2285-2300.
1010 Katz, A., 1973. The interaction of magnesium with calcite during crystal growth at
1011 25-90ºC and one atmosphere. Geochimia et Cosmochimica Acta 39, 486-508.
1012 Katz, B.G. and Bullen, T., 1996. The combined use of 87Sr/86Sr and carbon and
1013 water isotopes to study the hydrochemical interaction between groundwater and
1014 lakewater in mantled karst. Geochimia et Cosmochimica Acta, 60(24), 5075-5087.
1015 Khosravi, M., Rostami, B., Fatemi, S., 2012. Uncertainty Analysis of a Fractured
1016 Reservoir's Performance: A Case Study. Oil & Gas Science and Technology 67, 423-
1017 433.

1018 Kim, S.T., O'Neil, J.R., 1997. Equilibrium and nonequilibrium oxygen isotope
1019 effects in synthetic carbonates. Geochimia et Cosmochimica Acta 61, 3461-3475.
1020 Kinsman, D.J.J., 1969. Interpretation of Sr2+ concentrations in carbonate
1021 minerals and rocks. Journal of sedimentary Petrology 39, 486-508.
1022 Kolker, A., Chou, C.L., 1994. Cleat-Filling Calcite in Illinois Basin Coals: Trace-
1023 Element Evidence for Meteoric Fluid Migration in a Coal Basin. The Journal of Geology
1024 102.
1025 Lacroix, B., Baumgartner, L.P., Bouvier, A.S., Kempton, P.D., Vennemann, T.,
1026 2018. Multi fluid-flow record during episodic mode I opening: Amicrostructural and SIMS
1027 study (Cotiella Thrust Fault, Pyrenees). Earth and Planetary Science Letters 503, 37-46.
1028 Lacroix, B., Travé, A., Buatier, M., Labaume, P., Vennemann, T., Dubois, M.,
1029 2014. Syntectonic fluid-flow along thrust faults: Example of the South-Pyrenean fold-and-
1030 thrust belt. Marine and Petroleum Geology 49, 84-98.
1031 Lefticariu, L., Perry, E.C., Fischer, M.P., Banner, J.L., 2005. Evolution of fluid
1032 compartmentalization in a detachment fold complex. Geology 33, 69-72.
1033 Letouzey, J., Werner, P., Marty, A., 1990. Fault reactivation and structural
1034 inversion. Backarc and intraplate compressive deformations. Example of the eastern
1035 Sunda shelf (Indonesia). Tectonophysics 183, 341-362.
1036 Ligi, M., Bonatti, E., Cuffaro, M., Brunelli, D., 2013. Post-Mesozoic Rapid
1037 Increase of Seawater Mg/Ca due to Enhanced Mantle-Seawater Interaction. Scientific
1038 Reports 3, 2752.
1039 Linnemann, U. et al., 2018. New high-resolution age data from the Ediacaran–
1040 Cambrian boundary indicate rapid, ecologically driven onset of the Cambrian explosion.
1041 Terra Nova, 31, 49-58.
1042 López-Martínez, N., Fernández-Marrón, M.T., Valle, M.F., 1999. The succession
1043 of vertebrates and plants across the Cretaceous-Tertiary boundary in the Tremp
1044 Formation, Ager valley (south-central Pyrenees, Spain). Geobios 32, 617-627.

1045 Lorens, R., 1981. Sr, Cd, Mn and Co distribution coefficients in calcite as a
1046 function of calcite precipitation rate. Geochimia et Cosmochimica Acta 45, 553-561.
1047 Loveless, S., Bense, V., Turner, J., 2011. Fault architecture and deformation
1048 processes within poorly lithified rift sediments, Central Greece. Journal of Structural
1049 Geology 33, 1554-1568.
1050 Ludwig, K.R., 2009. Isoplot/Ex Ver 3.71: A geochronological toolkit for Microsoft
1051 Excel: Berkeley Geochronology Center Special Publications.
1052 Maher, H.D., Ogata, K., Braathen, A., 2017. Cone-in-cone and beef
1053 mineralization associated with Triassic growth basin faulting and shallow shale
1054 diagenesis, Edgeøya, Svalbard. Geological Magazine 154, 201-216.
1055 Marret, R., Allmendinger, R.W., 1990. Kinematic analysis of fault-slip data.
1056 Journal of Structural Geology 12, 973-986.
1057 Martínez-del Olmo, W., 2019. The Spanish petroleum systems and the
1058 overlooked areas and targets. Boletín Geológico y Minero, 130(2), 289-315.
1059 McArthur, J.M., Howarth, R.J., Bailey, T.R., 2001. Strontium Isotope Stratigraphy:
1060 LOWESS Version 3: Best Fit to the Marine Sr-Isotope Curve for 0–509 Ma and
1061 Accompanying Look-up Table for Deriving Numerical Age. Journal of Geology 109, 155-
1062 170.
1063 McCaig, A.M., Tritlla, J., Banks, D.A., 2000. Fluid mixing and recycling during
1064 Pyrenean thrusting: evidence from fluid inclusion halogen ratios. Geochimia et
1065 Cosmochimica Acta 64, 3395-3412.
1066 McCaig, A.M., Wayne, D.M., Marshall, J.D., Banks, D., Henderson, I., 1995.
1067 Isotopic and fluid inclusion studies of fluid movement along the Gavarnie Thrust, central
1068 Pyrenees: Reaction fronts in carbonate mylonites. American Journal of Science 295,
1069 309-343.
1070 McCrea, J.M., 1950. On the Isotopic Chemistry of Carbonates and a
1071 Paleotemperature Scale. Journal of Chemical Physics 18, 849-957.

McIntire, W.L., 1963. Trace element partition coefficients, a review of theory and applications to geology. Geochimia et Cosmochimica Acta 27, 1209-1264.

Mey, P.H.W., Nagtegaal, P.J.C., Roberti, K.J., Hartevelt, J.J.A., 1968. Lithostratigraphic subdivision of post-Hercinian deposits in the south-central Pyrenees, Spain. Leidse Geologische Mededelingen 41, 21-228.

Missenard, Y., Bertrand, A., Vergély, P., Benedicto, A., Cushing, M.-E., Rocher, M., 2014. Fracture-fluid relationships: implications for the sealing capacity of clay layers – Insights from field study of the Blue Clay formation, Maltese islands. Bulletin de la Société Géologique de France 185, 51-63.

Moeri, E.V., 1977. Oberkretazischen shelfsedimente in den zentralpyrenäen zwischen Rio Segre und Llobregat. Eclogae Geologicae Helvetiae 70, 193-235.

Muñoz, J.A., 1992. Evolution of a continental collision belt: ECORS–Pyrenees crustal balanced section, in: McClay, K.R. (Ed.), Thrust Tectonics. Chapman & Hall, London, pp. 235-246.

Muñoz, J.A., 2002. The Pyrenees, in: Gibbons, W., Moreno, T. (Eds.), The Geology of Spain. Geological Society, London, pp. 370-385.

Muñoz-López, D., Alías, G., Cruset, D., Cantarero, I., Travé, A., 2020. Influence of basement rocks on fluid evolution during multiphase deformation: the example of the Estamariu thrust in the Pyrenean Axial Zone. Solid Earth Discuss., in review, 2020, 1-39.

Nardini, N., Muñoz-López, D., Cruset, D., Cantarero, I., Martín-Martín, J.D., Benedicto, A., Gómez-Rivas, E., John, C.M., Travé, A., 2019. From early contraction to post-folding fluid evolution in the frontal part of the Bóixols thrust sheet (southern Pyrenees) as revealed by the texture and geochemistry of calcite cements. Minerals 9, 117.

Ogata, K., Senger, K., Braathen, A., Tveranger, J., 2014. Fracture corridors as seal-bypass systems in siliciclastic reservoir-cap rock successions: Field-based insights

1099 from the Jurassic Entrada Formation (SE Utah, USA). Journal of Structural Geology 66,
1100 162-187.
1101 Oms, O., Dinarés-Turell, J., Vicens, E., Estrada, R., Vila, B., Galobart, À., Bravo,
1102 A.M., 2007. Integrated stratigraphy from the Vallcebre Basin (southeastern Pyrenees,
1103 Spain): New insights on the continental Cretaceous−Tertiary transition in southwest
1104 Europe. Palaeogeography, Palaeoclimatology, Palaeoecology 255, 35-47.
1105 Paquette, J., and Reeder, R. J., 1995, Relationship between surface structure,
1106 growth mechanism, and trace element incorporation in calcite: Geochimia et
1107 Cosmochimica Acta, v. 59, p. 735-749.
1108 Petit, J.P., Beauchamp, J., 1986. Synsedimentary faulting and palaeocurrent
1109 patterns in the Triassic sandstones of the High Atlas (Morocco). Sedimentology 33, 817-
1110 829.
1111 Petit, J.P., Laville, E., 1987. Morphology and microstructures of hydroplastic
1112 slickensides in sandstone. Geological Society, London, Special Publications 29, 107-
1113 121.
1114 Pons, J.M., Caus, E., 1996. El Cretácico Superior en el Pirineo. Paleontología.
1115 Revista Española de Paleontología 11, 182-189.
1116 Puigdefàbregas, C., Muñoz, J.A., Marzo, M., 1986. Thrust Belt Development in
1117 the Eastern Pyrenees and Related Depositional Sequences in the Southern Foreland
1118 Basin, in: Allen, P.A., Homewood, P. (Eds.), Foreland Basins. Blackwell Publishing Ltd.,
1119 Oxford, UK. , pp. 229-246.
1120 Puigdefàbregas, C., Muñoz, J.A., Vergés, J., 1992. Thrusting and Foreland Basin
1121 Evolution in the Southern Pyrenees, in: McClay, K.R. (Ed.), Thrust Tectonics. London,
1122 Chapman & Hall, pp. 247-254.
1123 Reeder, R. J., and Grams, J. C., 1987, Sector zoning in calcite cement crystals:
1124 implications for trace element distributions in carbonates: Geochimia et Cosmochimica
1125 Acta, v. 51, p. 187-194.

Ring, U. and Gerdes, A., 2016. Kinematics of the Alpenrhein-Bodensee graben system in the Central Alps: Oligocene/Miocene transtension due to formation of the Western Alps arc. Tectonics, 35, 1367-1391.

Roberts, N.M.W., Rasbury, E. T., Parrish, R., Smith, C. J., Horstwood, M. S. A., Condon, D. J., 2017. A calcite reference material for LA-ICP-MS U-Pb geochronology. Geochemistry, Geophysics, Geosystems, 18, 2807-2814.

Rosell, J., Linares, R., Llompart, C., 2001. El "Garumniense" prepirenaico. Rev. Soc. Geol. España 14, 47-56.

Roure, F., Choukroune, P., Berastegui, J., Muñoz, J.A., Villien, A., Matheron, P., Bareyt, M., Seguret, M., Camara, P., Deramond, J., 1989. Ecors deep seismic data and balanced cross sections: Geometric constraints on the evolution of the Pyrenees. Tectonics 8, 41-50.

Roure, F., Swennen, R., Schneider, F., Faure, J.L., Ferket, H., Guilhaumou, N., Osadetz, K., Robion, P., Vandeginste, V., 2005. Incidence and Importance of Tectonics and Natural Fluid Migration on Reservoir Evolution in Foreland Fold-and-Thrust Belts. Oil & Gas Science and Technology 60, 67-106.

Rutqvist, J., Rinaldi, A.P., Cappa, F., Moridis, G.J., 2013. Modeling of fault reactivation and induced seismicity during hydraulic fracturing of shale-gas reservoirs. Journal of Petroleum Science and Engineering 107, 31-44.

Sans, M., Muñoz, J.A., Vergés, J., 1996. Triangle zone and thrust wedge geometries related to evaporitic horizons (Southern Pyrenees). Canadian Petroleum Geology Bulletin 4, 375-384.

Séguret, M., 1972. Étude tectonique des nappes et séries décollées de la partie centrale du vesant sud des Pyrénées. Pub. USTELA, sér, Geol. Struct. n.2, Montpellier.

Shackleton, J.R., Cooke, M.L., Sussman, A.J., 2005. Evidence for temporally changing mechanical stratigraphy and effects on joint-network architecture. Geology 33, 101-104.

1153 Shackleton, J.R., Cooke, M.L., Vergés, J., Simó, T., 2011. Temporal constraints
1154 on fracturing associated with fault-related folding at Sant Corneli anticline, Spanish
1155 Pyrenees. Journal of Structural Geology 33, 5-19.
1156 Shariatinia, Z., Haghighi, M., Feiznia, S., Alizai, A.H., Levresse, G., 2013.
1157 Hydrocarbon migration in the Zagros Basin, offshore Iran, for understanding the fluid flow
1158 in the Oligocene–Miocene carbonate reservoirs. Russian Geology and Geophysics 54,
1159 64-81.
1160 Sibson, R.H., 1995. Selective fault reactivation during basin inversion: potential
1161 for fluid redistribution through fault-valve action, in: Buchanan, J.G., Buchanan, P.G.
1162 (Eds.), Basin Inversion, Geological Society Special Publication, pp. 3-19.
1163 Simó, A., 1985. Secuencias deposicionales del Cretácico superior de la unidad
1164 del Montsec (Pirineo Central), Tesis Doctoral, Universitat de Barcelona. 325 pp.
1165 Soliva, R. and Benedicto, A., 2004. A linkage criterion for segmented normal
1166 faults. Journal of Structural Geology, 26, 2251-2267.
1167 Soliva, R. and Benedicto, A., 2005. Geometry, scaling relations and spacing of
1168 vertically restricted normal faults. Journal of Structural Geology, 27, 317-325.
1169 Soliva, R., Benedicto, A., Maerten, L., 2006. Spacing and linkage of confined
1170 normal faults: Importance of mechanical thickness. Journal of Geophysical Research
1171 111, B01402.
1172 Soliva, R., Benedicto, A., Schultz, R.A., Maerten, L., Micarelli, L., 2008.
1173 Displacement and interaction of normal fault segments branched at depth: Implications
1174 for fault growth and potential earthquake rupture size. Journal of Structural Geology 30,
1175 1288-1299.
1176 Soumaya, A., Ayed, N.B., Delvaux, D., Ghanmi, M., 2015. Spatial variation of
1177 present-day stress field and tectonic regime in Tunisia and surroundings from formal
1178 inversion of focal mechanisms: Geodynamic implications for central Mediterranean.
1179 Tectonics 34, 1154-1180.

Steuber, T., Rauch, M., 2005. Evolution of the Mg/Ca ratio of Cretaceous seawater: Implications from the composition of biological low-Mg calcite. Marine Geology 217, 199-213.

Sugrañes, L.S., Clavell, E., 1973. Nota sobre la edad y posición tectóiiica de los conglomerados eocenos de Queralt (Prepirineo oriental, Prov. de Barcelona) Acta Geologica Hispanica 8, 1-6.

Tavani, S., Mencos, J., Bausà, J., Muñoz, J.A., 2011. The fracture pattern of the Sant Corneli Bóixols oblique inversion anticline (Spanish Pyrenees). Journal of Structural Geology 33, 1662-1680.

Tavani, S., Storti, F., Lacombe, O., Corradetti, A., Muñoz, J.A., Mazzoli, S., 2015. A review of deformation pattern templates in foreland basin systems and fold-and-thrust-belts: Implications for the state of stress in the frontal regions of thrust wedges. Earth-Science Reviews 141, 82-104.

Tindall, J., Flecker, R., Valdes, P., Schmidt, D.N., Markwick, P., Harris, J., 2010. Modelling the oxygen isotope distribution of ancient seawater using a coupled ocean–atmosphere GCM: Implications for reconstructing early Eocene climate. Earth and Planetary Science Letters 292, 265-273.

Travé, A., Labaume, P., Calvet, F., Soler, A., 1997. Sediment dewatering and pore fluid migration along thrust faults in a foreland basin inferred from isotopic and elemental geochemical analyses (Eocene southern Pyrenees, Spain). Tectonophysics 282, 375-398.

Travé, A., Labaume, P., Calvet, F., Soler, A., Tritlla, J., Bautier, M., Potdevin, J.L., Séguret, M., Raynaud, S., Briqueu, L., 1998. Fluid migration during Eocene thrust emplacement in the south Pyrenean foreland basin (Spain): an integrated structural, mineralogical and geochemical approach, in: Mascle, A., Puigdefàbregas, C., LuterBacher, H.P., Fernàndez, M. (Eds.), Cenozoic Foreland Basins of Western Europe. Geological Society, Special Publications, pp. 163-188.

1207 Travé, A., Calvet, F., Sans, M., Vergés, J., Thirlwall, M., 2000. Fluid history
1208 related to the Alpine compression at the margin of the south-Pyrenean Foreland basin:
1209 the El Guix anticline. Tectonophysics 321, 73-102.
1210 Trincal, V., Buatier, M., Charpentier, D., Lacroix, B., Lanari, P., Labaume, P.,
1211 Lahfid, A., Venneman, T., 2017. Fluid–rock interactions related to metamorphic reducing
1212 fluid flow in meta-sediments: example of the Pic-de-Port-Vieux thrust (Pyrenees, Spain).
1213 Contributions to Mineralogy and Petrology 172, 78.
1214 Tucker, M.E., Wright, P.V., 1990. Carbonate Sedimentology. Blackwell, Oxford.
1215 Vaks, A. et al., 2003. Paleoclimate reconstruction based on the timing of
1216 speleothem growth and oxygen and carbon isotope composition in a cave located in the
1217 rain shadow in Israel. Quaternary Research, 59(2), 182-193.
1218 Vandeginste, V. et al., 2007. Geochemical constraints on the origin of the Kicking
1219 Horse and Monarch Mississippi Valley-type lead-zinc ore deposits, southeast British
1220 Columbia, Canada. Mineralium Deposita, 42, 913-935.
1221 Vandeginste, V., Swennen, R., Allaeys, M., Ellam, R.M., Osadetz, K., Roure, F.,
1222 2012. Challenges of structural diagenesis in foreland fold-and-thrust belts: A case study
1223 on paleofluid flow in the Canadian Rocky Mountains West of Calgary. Marine and
1224 Petroleum Geology 35, 235-251.
1225 Veizer, J. and Hoefs, J., 1976. Nature of O^{18}/O^{16} and C^{13}/C^{12} Secular Trends in
1226 Sedimentary Carbonate Rocks. Geochimia et Cosmochimica Acta, 40, 1387-1395.
1227 Veizer, J., Ala, D., Azmy, K., Bruckschen, P., Buhl, D., Bruhn, F., Carden,G.A.F.,
1228 Diener, A., Ebneth, S., Godderis, Y., Jasper, T., Korte, C., Pawellek, F., Podlaha, O. G.,
1229 Strauss, H., 1999. $^{87}Sr/^{86}Sr$, $\delta^{13}C$ and $\delta^{18}O$ evolution of Phanerozoic seawater. Chemical
1230 Geology, 161, 59-88.
1231 Vergés, J., 1993. Estudi geològic del vessant sud del Pirineu oriental i central.
1232 Evolució cinemàtica en 3D. PhD thesis, Universitat de Barcelona, Barcelona, Spain, p.
1233 203.

1234 Vergés, J., Muñoz, J.A., 1990. Thrust sequences in the southern central
1235 Pyrenees. Bull. Soc. géol. France 8, 265-271.
1236 Vergés, J., Martínez, A., Muñoz, J.A., 1992. South Pyrenean fold and thrust belt:
1237 The role of foreland evaporitic levels in thrust geometry, in: McClay, K. (Ed.), Thrust
1238 Tectonics. London, Chapman & Hall, pp. 255-264.
1239 Vergés, J. et al., 1995. Eastern Pyrenees and related foreland basins: pre-, syn-
1240 and post-collisional crustal-scale cross-sections. Marine and Petroleum Geology, 12(8),
1241 893-915.
1242 Vergés, J. et al., 1998. Quantified vertical motions and tectonic evolution of the
1243 SE Pyrenean foreland basin. In: A. Mascle, C. Puigdefàbregas, H.P. Luterbacher and M.
1244 Fernàndez (Eds.), Cenozoic Foreland Basins of Western Europe. Geological Society
1245 Special Publications, pp. 107-134.
1246 Vergés, J., Fernàndez, M., Martínez, A., 2002. The Pyrenean orogen: pre-, syn-,
1247 and post-collisional evolution, in: Rosenbaum, G., Lister, G. (Eds.), Reconstruction of the
1248 evolution of the Alpine-Himalayan Orogen. Journal of the Virtual Explorer, pp. 55-74.
1249 Vilasi, N., 2010. Study of reservoir analogues in foreland fold-and-thrust belts:
1250 sedimentology, diagenesis, deformation and fracturing of the upper cretaceous-eocene
1251 carbonate systems of the ionian zone (Southern Albania). PhD thesis. Ecole des Mines
1252 de Paris, Paris, France, p. 190.
1253 Vilasi, N., Swennen, R. and Roure, F., 2006. Diagenesis and fracturing of
1254 Paleocene-Eocene carbonate turbidite systems in the Ionian Basin: The example of the
1255 Kelçyra area (Albania). Journal of Geochemical Exploration, 89, 409-413.
1256 Watkins, H., Healy, D., Bond, C.E., Butler, R.W.H., 2018. Implications of
1257 heterogeneous fracture distribution on reservoirquality; an analogue from the Torridon
1258 Group sandstone, MoineThrust Belt, NW Scotland. Journal of Structural Geology 108,
1259 180-197.
1260 Wiprut, D., Zoback, M.D., 2000. Fault reactivation and fluid flow along a
1261 previously dormant normal fault in the northern North Sea. Geology 27, 595-598.

1262 Wiseall, A.C., Cuss, R.J., Hough, E., Kemp, S.J., 2018. The role of fault gouge
1263 properties on fault reactivation during hydraulicstimulation; an experimental study using
1264 analogue faults. Journal of Natural Gas Science and Engineering 59, 21-34.
1265 Zheng, Y.F. and Hoefs, J., 1993. Carbon and oxygen isotopic covariations in
1266 hydrothermal calcites. Mineralium Deposita, 28, 79-89.

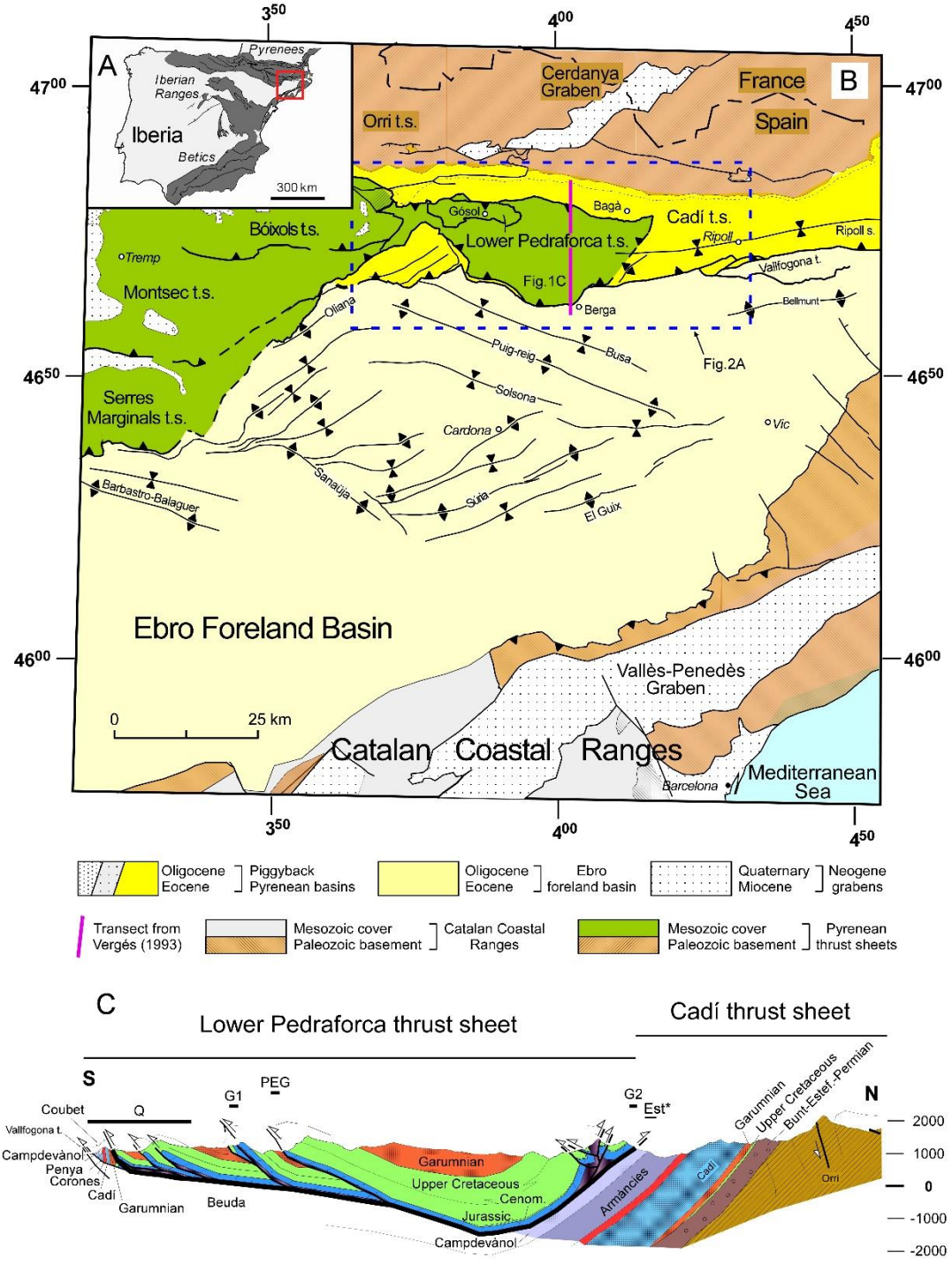

Fig. 1 A) Regional map of the Iberian Peninsula showing the location of the South Pyrenean fold and thrust belt (red box). B) Simplified geological map showing the main structural units forming the South Pyrenean fold and thrust belt (Vergés, 1993). The thick pink line indicates the location of the cross-section shown in Fig. 1C. The dashed blue box indicates the location of Fig. 2A. C) Geological cross-section of the Lower Pedraforca

1273 thrust sheet from Vergés (1993) showing the structural position of the studied localities.

1274 Est*: projection of the position of this location.

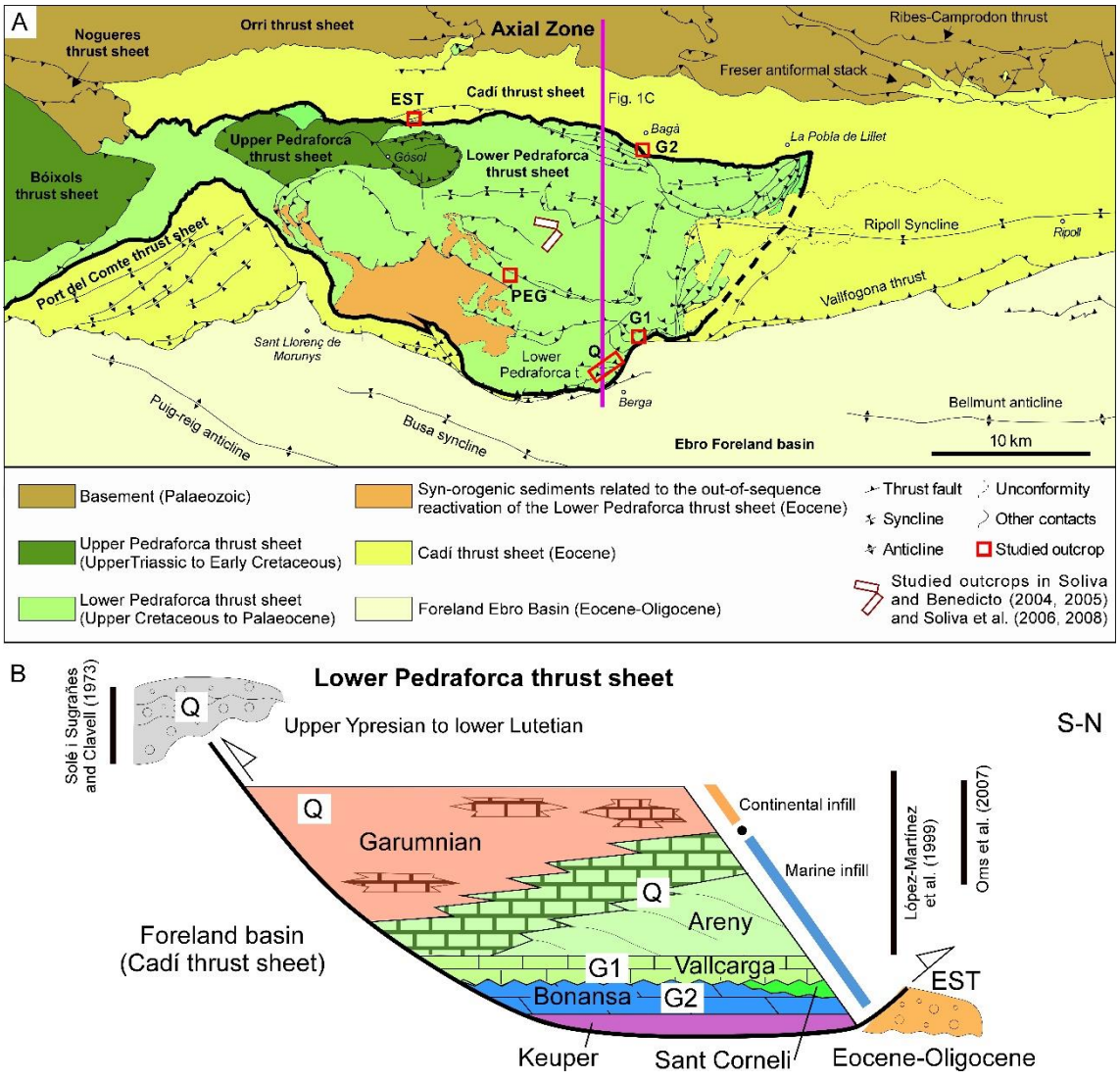

Fig. 2 A) Structural sketch of the studied area with locality locations. White boxes bounded by red lines indicate the areas studied by Soliva and Benedicto (2004, 2005) and Soliva et al. (2006, 2008) in the Lower Pedraforca thrust sheet. The thick pink line indicates the location of the cross-section shown in Fig. 1C. B) N-S stratigraphic panel of the Lower Pedraforca sheet. The age of sedimentary units has been defined according to Solé i Sugrañes and Clavell (1973), López-Martínez et al. (1999) and Oms et al. (2007).

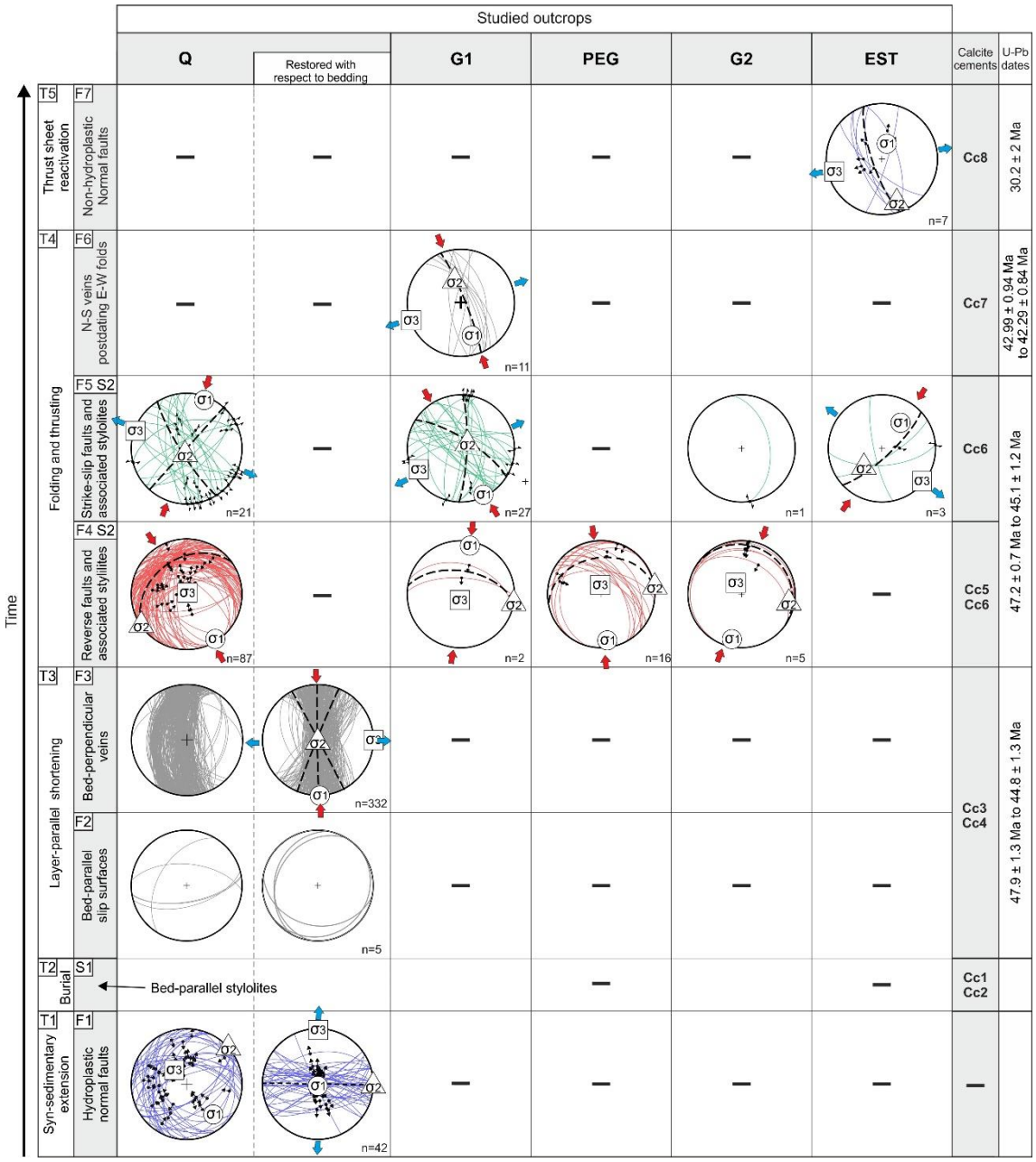

Fig. 3 Lower hemisphere Schmidt stereoplots representing fracture data from the different studied localities, their associated calcite cement and different stages of deformation and stylolitization. Fracture systems F1, F2 and F3 are presented at their current orientation and restored with respect to bedding. The grey boxes with references Q, G1, PEG, G2 and EST represent the studied localities in Figs. 1 and 2. Thick dashed black lines represent mean planes for each fracture system.

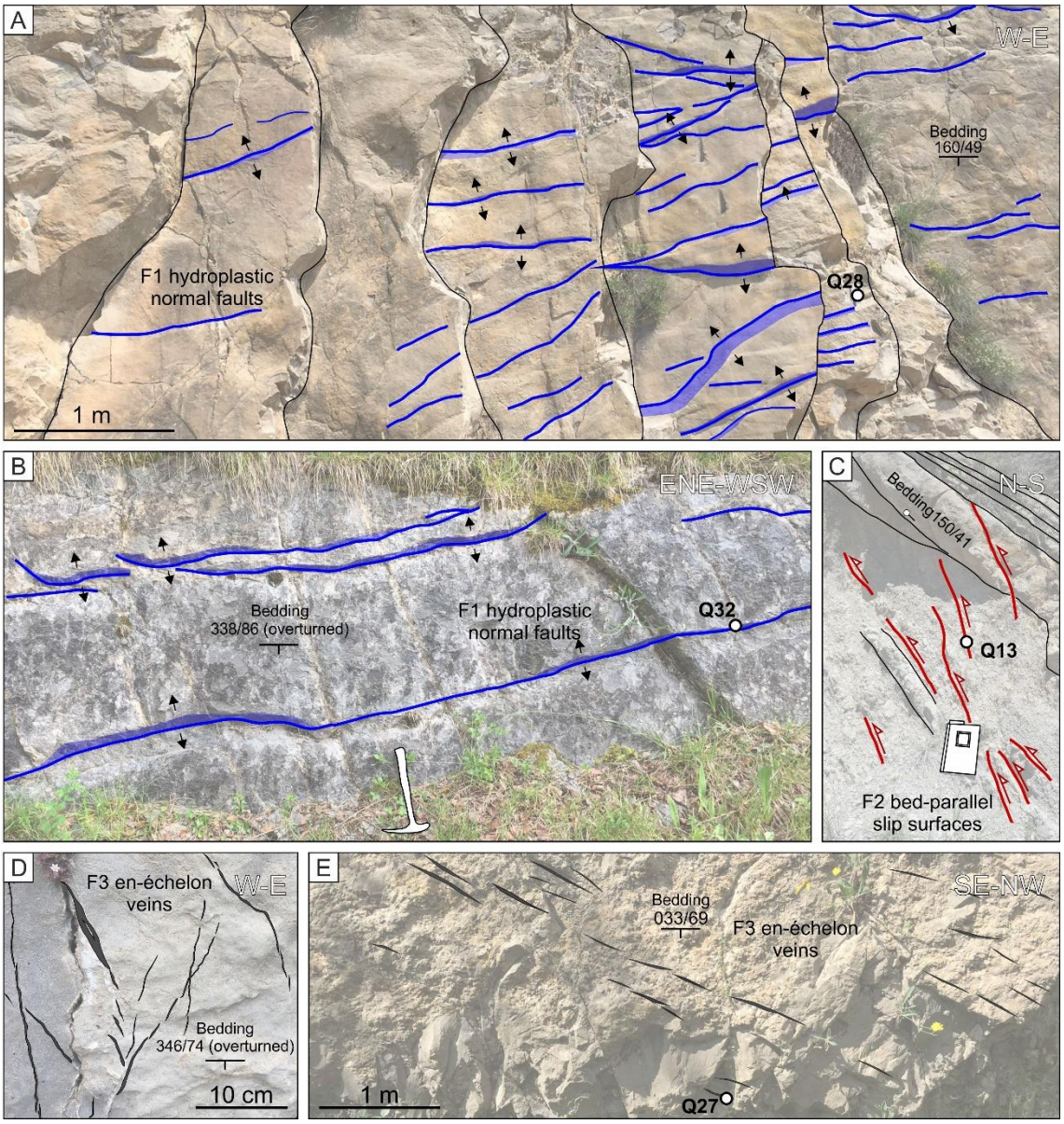

Fig. 4 Outcrop images showing the main features of fracture systems F1, F2 and F3 within the Lower Pedraforca thrust sheet. A-B) E-W hydroplastic normal faults F1 in the Upper Cretaceous Areny Formation and middle Eocene syn-orogenic sediments, respectively. C) Bed-parallel slip surfaces F2 affecting Palaeocene sediments. D-E) N-S, NNW-SSE and NNE-SSW en-échelon vein arrays F3 affecting middle Eocene syn-orogenic sediments and the Upper Cretaceous Areny Formation, respectively. Bed dip directions and dips are given. White points indicate sample location.

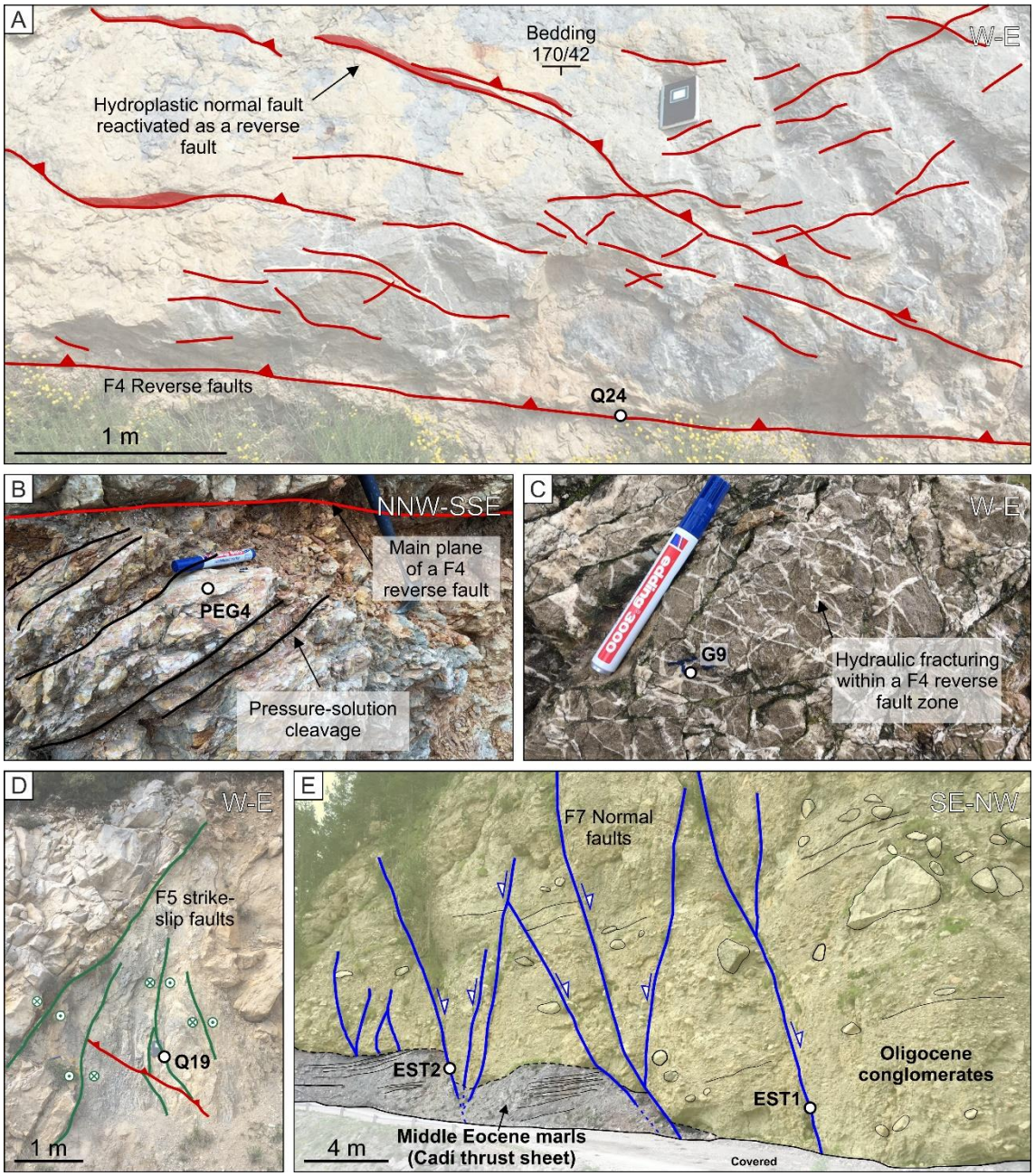

1298

1299 **Fig. 5** Outcrop images showing the main features of fracture systems F4, F5 and F7
1300 within the Lower Pedraforca thrust sheet. A) Reverse faults F4 and associated veins
1301 within the Upper Cretaceous Areny Formation. Bed dip direction and dip is given. B)
1302 Pressure solution cleavage formed in the core of a F4 thrust fault. C) Hydraulic fracturing
1303 formed in the damage zone of a F4 thrust fault. D) F5 strike-slip faults affecting the Upper
1304 Cretaceous Areny Formation. E) F7 normal faults affecting Oligocene conglomerates.
1305 White points indicate sample location.

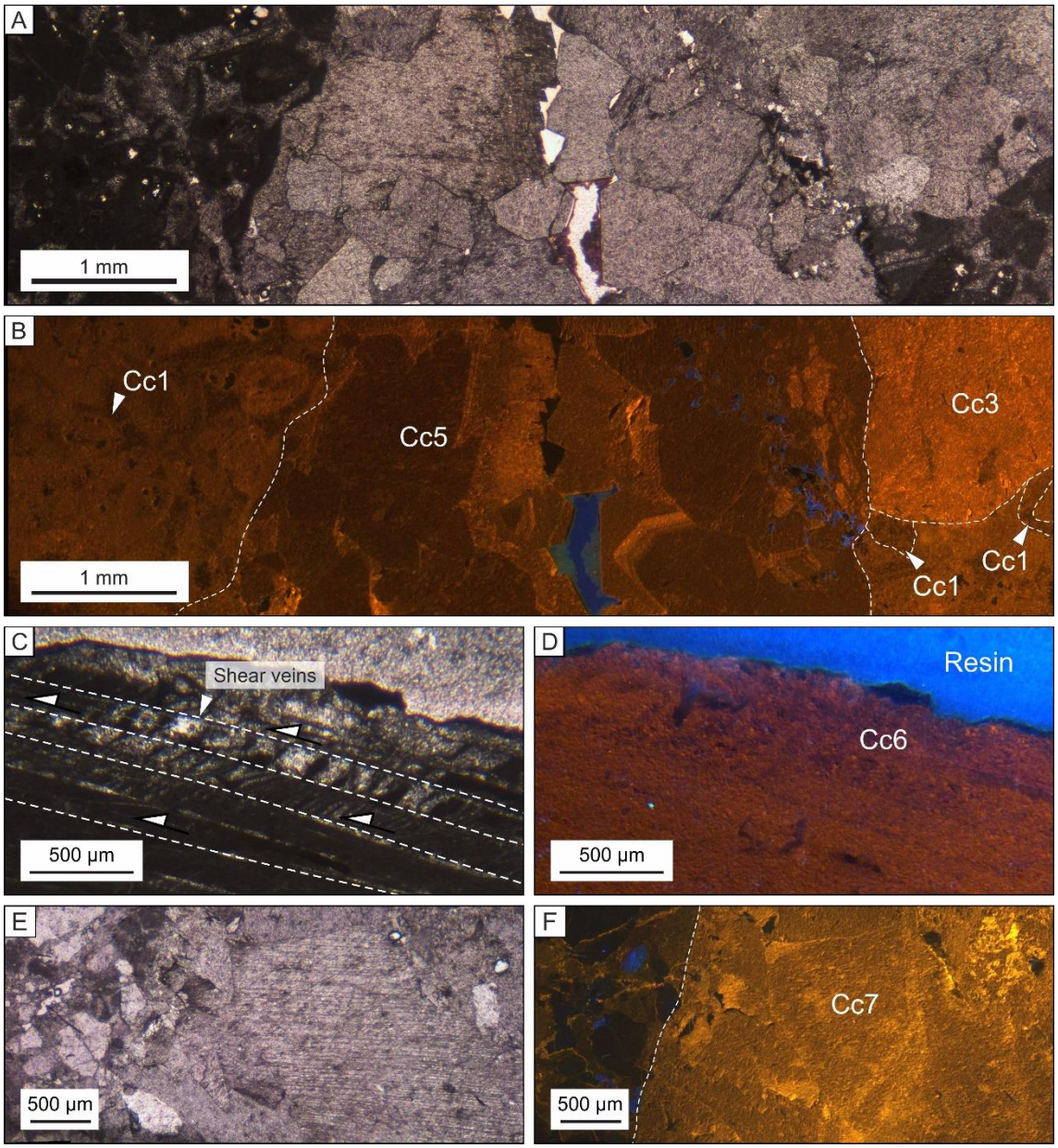

Fig. 6 Images from polarizing optical and cathodoluminescence (CL) microscopy of the main features of calcite cement and microstructures. A-B) Crosscutting relationships between intergranular porosity and veins filled with calcite cement Cc3 and Cc5. C-D) Image showing veins filled with calcite cement Cc6 in F4 reverse faults. E-F) Calcite cement Cc8 filling veins in F7 normal faults.

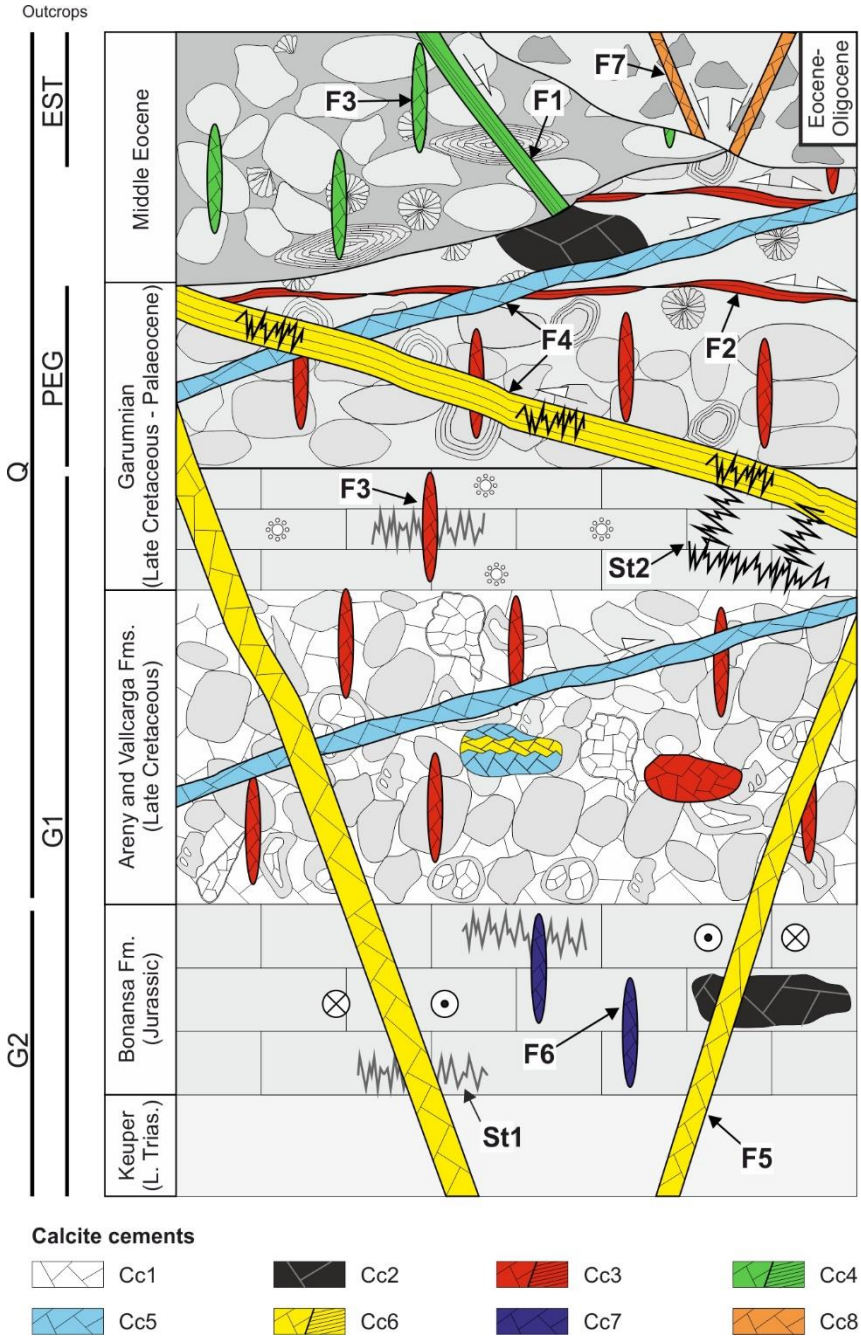

1312

1313 **Fig. 7** Schematic representation of the crosscutting relationships between fractures,

1314 stylolites and related calcite cement in the Lower Pedraforca thrust sheet.

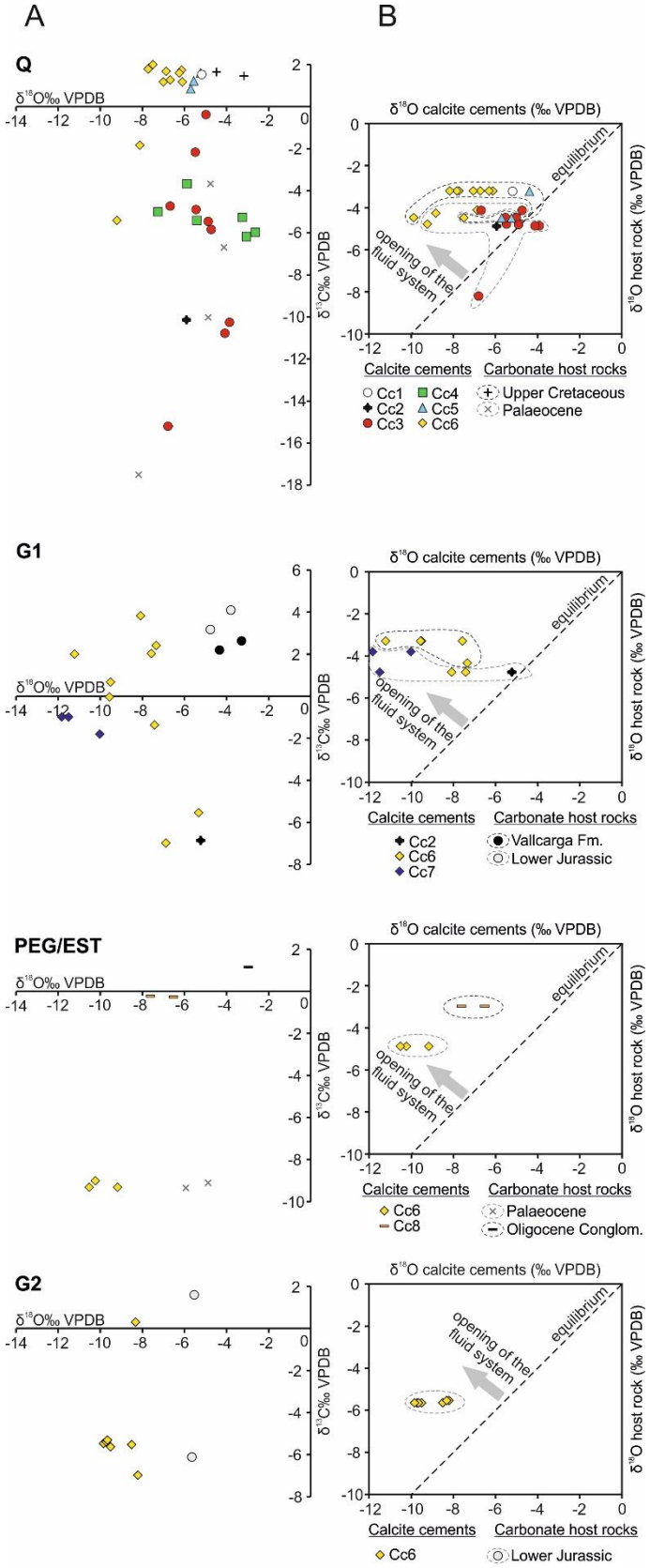

1315

1316 **Fig. 8** A) $\delta^{18}O$ vs $\delta^{13}C$ from the Lower Pedraforca thrust sheet. B) Cross-plots comparing

1317 the $\delta^{18}O$ of calcite cement with their adjacent host rocks. The dashed areas group

cement according to their adjacent host rocks. The dashed black line represents the equilibrium between calcite veins and their adjacent host rocks.

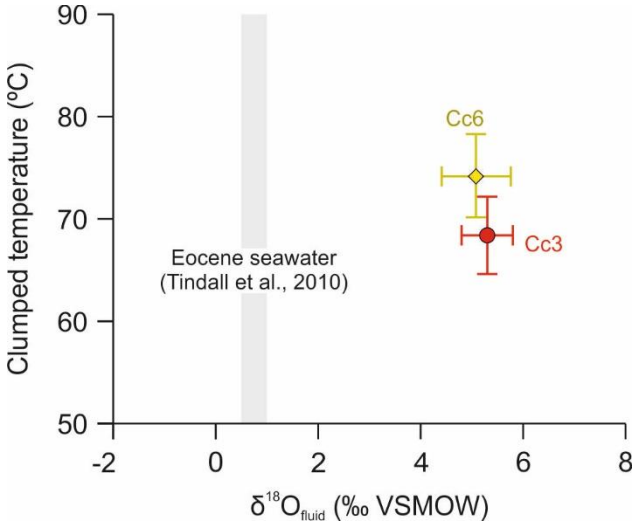

Fig. 9 Clumped isotope temperatures in ºC vs calculated $\delta^{18}O_{fluid}$ (‰ VSMOW) for calcite cement Cc3 and Cc6. $\delta^{18}O$ of Eocene seawater according to Tindall et al. (2010).

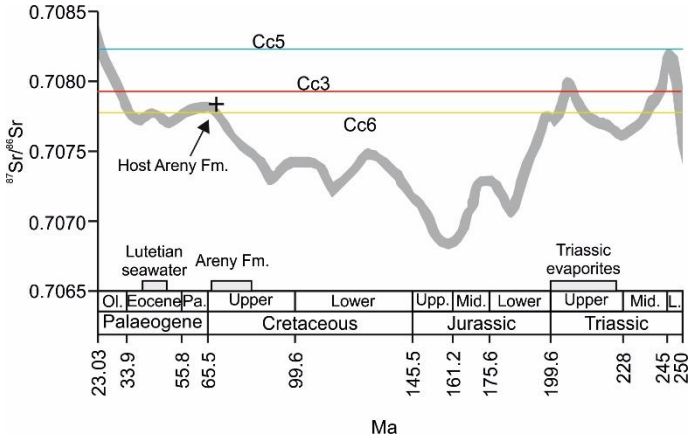

1323

1324 **Fig. 10** $^{87}Sr/^{86}Sr$ composition of calcite cement and carbonate host rocks. The $^{87}Sr/^{86}Sr$

1325 ratios of the LOWESS curve from McArthur et al. (2001) are also plotted. The grey area

1326 boxes indicate the $^{87}Sr/^{86}Sr$ ratio of middle Eocene and Upper Triassic seawater from

1327 McArthur et al. (2001).

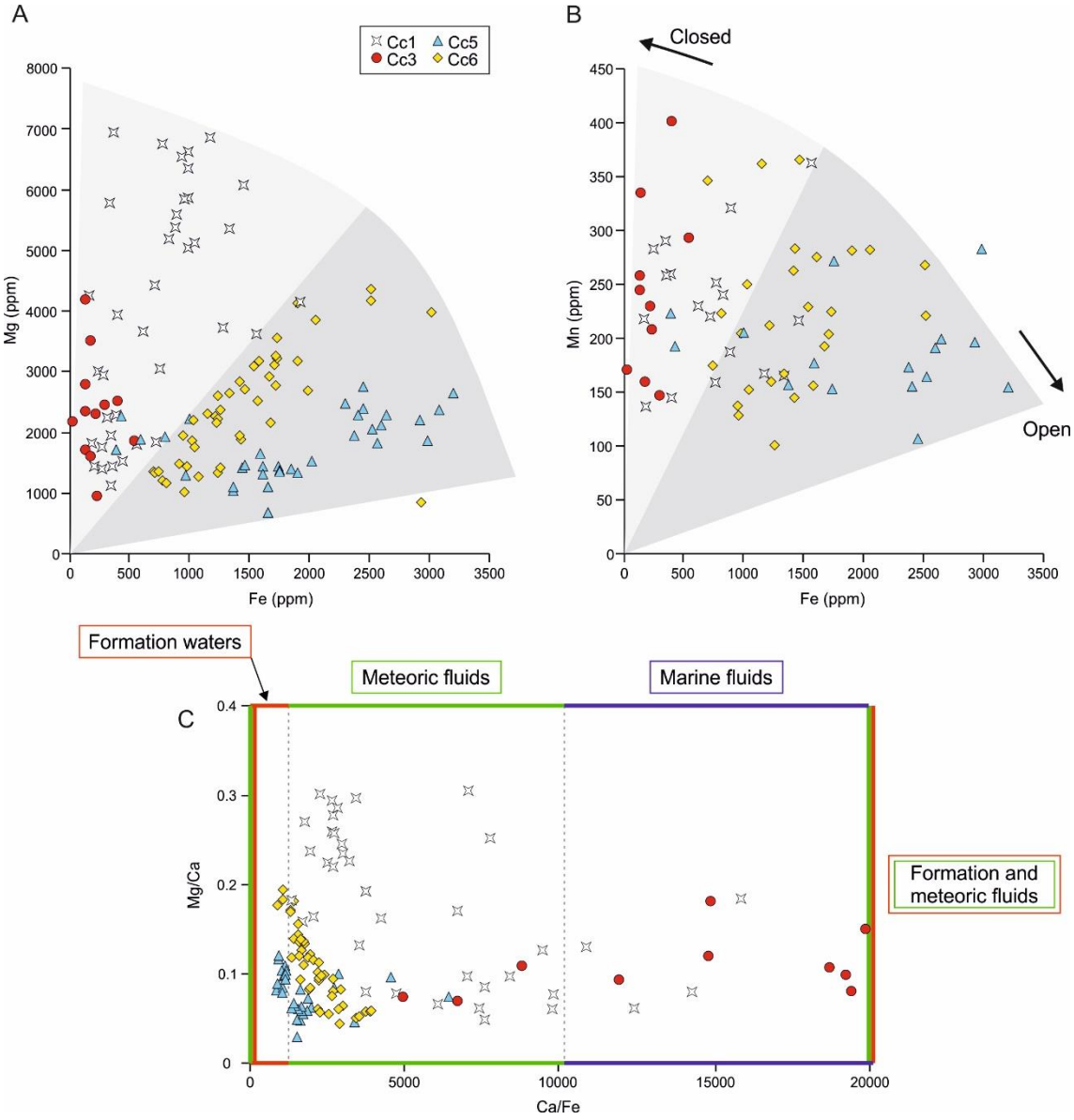

Fig. 11 Elemental composition of the calcite cement. A-B) Fe vs Mg and Fe vs Mn cross-plots of calcite cement Cc1, Cc3, Cc5 and Cc6. C) Ca/Fe vs Mn/Ca molar ratios cross-plot of calcite cement Cc1, Cc3, Cc5 and Cc6. Areas bounded by blue, green and red thick lines represent the composition of marine, meteoric and formation fluids, respectively. Fluid compositions are based on McIntire (1963), Howson et al. (1987), Tucker and Wright (1990), Kolker and Chou (1994), Steuber and Rauch (2005) and Ligi et al. (2013).

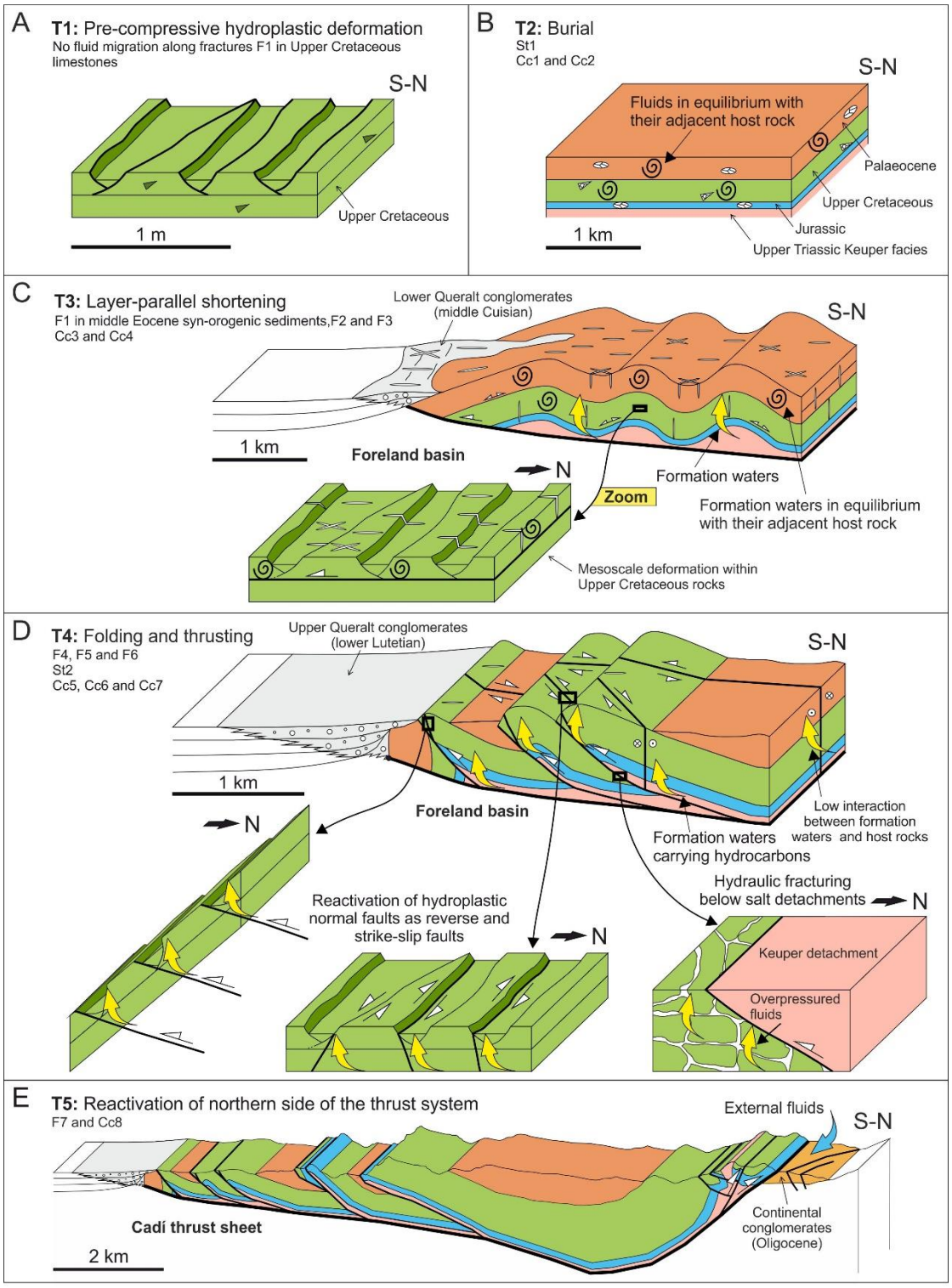

Fig. 12 Fluid flow evolution during the emplacement of the Lower Pedraforca thrust sheet. A) T1, pre-compressive hydroplastic deformation. B) T2, burial diagenesis. C) T3, layer-parallel shortening. D) T4, folding and thrusting. E) T5, reactivation of the northern sector of the thrust system. For each stage, the type of migrating fluids, associated calcite cement and fractures are given.

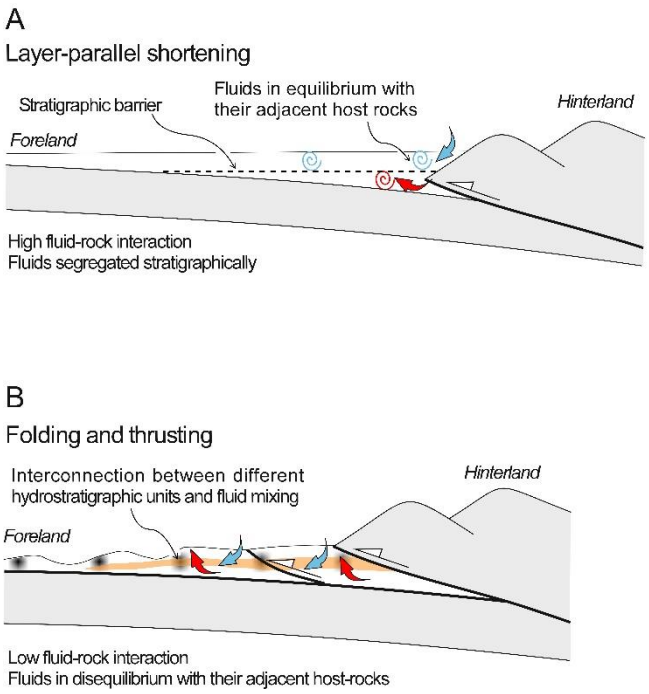

1342

1343 **Fig. 13** Conceptual model of fluid flow in fold and thrust belts. A) Layer-parallel
1344 shortening stage. Fluids are in equilibrium with their adjacent host rock and fluid-host
1345 rock interaction is high. Fluids are segregated stratigraphically. B) Folding and thrusting
1346 stage. The paleohydrological system opens, allowing the interconnection between
1347 different hydrostratigraphic units and fluid mixing. The fluid-host rock interaction is low.

Table 1. U-Pb dates of calcite cement Cc3, Cc4, Cc6, Cc7 and Cc8.

Sample	Locality	Fracture set	Cement type	Age (Ma)	± 2σ	MSWD	$^{207}Pb/^{206}Pb$ Upper intercepts	± 2σ	Number of spots
Q27	Q	F3	Cc3	45.7	1.9	2.2	0.845	0.033	25
Q3-1	Q	F4	Cc3	47.3	1	1.3	0.879	0.036	24
Q11	Q	F3	Cc4	47.9	1.3	1.7	0.827	0.03	31
Q33	Q	F3	Cc4	44.8	1.3	1.4	0.8756	0.0062	23
Q24	Q	F4	Cc6	45.1	1.2	1.09	0.8327	0.0028	32
Q29	Q	F4	Cc6	47.2	0.7	1.4	0.829	0.013	27
G3	G1	F6	Cc7	42.9	0.9	1.8	0.705	0.004	32
G3b	G1	F6	Cc7	42.3	0.8	1.5	0.8091	0.0043	20
EST2	EST	F7	Cc8	30.2	2	1.8	0.843	0.011	21

Table 2. $\delta^{13}C$, $\delta^{18}O$, Δ_{47} and $\delta^{18}O_{fluid}$ of the calcite cement Cc3 and Cc6 within the Lower Pedraforca thrust sheet. n represents the number of analyses per sample.

Sample	Locality	Cement type	n	$\delta^{13}C$ ‰ VPDB[a]	$\delta^{18}O$ ‰ VPDB[a]	Δ_{47}[b]	T ºC	$\delta^{18}O_{fluid}$ ‰ VSMOW
Q2	Q	Cc3	4	+0.33 (0.01)	-5.02 (0.06)	0.579 ± 0.011	69.1 ± 5.3	+5.4 ± 0.9
Q24	Q	Cc6	3	+1.6 (0.04)	-6.1 (0.03)	0.569 ± 0.008	74.2 ± 4	+5.1 ± 0.7

[a] 1σ error for $\delta^{13}C$ and $\delta^{18}O$ of calcite cement.

[b] Error for Δ47 is presented as standard error and calculated by the replicate standard deviation divided by square root of n.

Table 3. Mg/Ca, Sr/Ca, Ca/Fe and Mn/Ca ratios for calcite cement Cc1, Cc3, Cc4, Cc5 and Cc6 precipitated in locality Q.

Cement type	Mg/Ca		Sr/Ca		Ca/Fe		Mn/Ca	
Cc1	Max.	0.304	Max.	0.052	Max.	15903	Max.	0.000085
	Min.	0.047	Min.	0.006	Min.	1390	Min.	0.000033
	Mean	0.175	Mean	0.014	Mean	5570	Mean	0.000053
Cc3	Max.	0.18	Max.	0.013	Max.	19934	Max.	0.000111
	Min.	0.069	Min.	0.006	Min.	4963	Min.	0.000032
	Mean	0.011	Mean	0.008	Mean	13357	Mean	0.000054
Cc4	Max.	0.197	Max.	0.020	Max.	-	Max.	0.000091
	Min.	0.034	Min.	0.007	Min.	-	Min.	0.000033
	Mean	0.104	Mean	0.01	Mean	-	Mean	0.000048
Cc5	Max.	0.121	Max.	0.027	Max.	6993	Max.	0.000086
	Min.	0.03	Min.	0.005	Min.	836	Min.	0.000025
	Mean	0.078	Mean	0.015	Mean	1916	Mean	0.000051
Cc6	Max.	0.194	Max.	0.019	Max.	3912	Max.	0.000083
	Min.	0.044	Min.	0.006	Min.	880	Min.	0.000023
	Mean	0.107	Mean	0.011	Mean	2149	Mean	0.000049